

1 **Aggregation of Slightly Buoyant Microplastics in Three-Dimensional Vortex Flows**

2 Irina I. Rypina¹, Larry J. Pratt¹, and Michael Dotzel¹

3 ¹ Woods Hole Oceanographic Institution, Physical Oceanography Department, 266 Woods Hole
4 Rd., Woods Hole, MA 02543

5 Corresponding author email: irypina@whoi.edu

6

7

8

9

10

11

12

13

14

15

16

17

18

19 **Abstract**

20 Although the movement and aggregation of microplastics at the ocean surface has been well
21 studied, less is known about the subsurface. Within the Maxey-Riley framework governing the
22 movement of small rigid spheres with high drag in fluid, aggregation of buoyant particles is
23 encouraged in vorticity-dominated regions. We explore this process in an idealized model that is
24 qualitatively reminiscent of a three-dimensional eddy with an azimuthal and overturning
25 circulation. In the axially symmetric state, buoyant spherical particles that do not accumulate at
26 the top boundary are attracted to a loop consisting of periodic orbits. Such a loop exists when
27 drag on the particle is sufficiently strong. For small slightly-buoyant particles, this loop is located
28 close to the periodic fluid parcel trajectory. If the symmetric flow is perturbed by a symmetry-
29 breaking disturbance, additional attractors for small rigid slightly-buoyant particles may arise
30 near periodic orbits of fluid parcels within the resonance zones created by the disturbance.
31 Disturbances with periodic or quasi-periodic time dependence may produce even more attractors,
32 with a shape and location that recurs periodically. However, not all such loops attract, and rigid
33 particles released in the vicinity of one loop may instead be attracted to a nearby attractor.
34 Examples are presented along with mappings of the respective basins of attraction.

35

36

37

38

39

40 **Significance statement**

41 This paper investigates aggregation of small, spherical, slightly buoyant, rigid particles in a
42 simple three-dimensional vortex flow. Our goal was to gain insights into the behaviour of
43 slightly buoyant marine microplastics in a flow that qualitatively resembles ocean eddies.
44 Attractors are mapped out for the steady axisymmetric, steady asymmetric, and non-steady
45 asymmetric vortices over a range of flow and particle parameters. Simple theoretical arguments
46 are used to interpret the results.

47

48

49

50

51

52

53

54

55

56

57

58 **I. Introduction**

59 Marine microplastic pollution has been a rising concern for the ocean environmental and for
60 human health. Microplastics (scales < 5mm) and nanoplastics (scales < 1 μm) have been found
61 in the tissues of marine animals, some of which are consumed by humans (Landrigan, et al.
62 2023). This comes at a time when global production of plastics is projected to increase.
63 Observations of marine microplastics have been conventionally carried out using net tows and
64 mostly occurred at or near the sea surface (van Sebille et al., 2015). However, the density of
65 many types of microplastic particles, including high-density polyethylene, is sufficiently close to
66 that of sea water that suspension within the water column for long periods of time is feasible. For
67 the near-surface microplastics, Kukulka et al. (2010) and Kooi et al. (2016) present observational
68 evidence for the fast decay in concentrations with depth over the top 5 – 20 m of the water
69 column, with the vertical penetration of plastic particles dependent on the wind speed.
70 Pabortsava and Lampitt (2020), on the other hand, show observational evidence for much deeper,
71 below-the-mixed-layer subsurface peaks for three common types of microplastics in the Atlantic
72 Ocean. Processes such as biofouling and bio-geo-chemical or photo degradation might increase
73 the density of the plastic particles and eventually lead to the sinking of microplastics from the
74 surface into the deeper part of the water column (Kaiser et al., 2017; Kreczak et al., 2021; Kvale
75 et al., 2020). Consumption by biomass with the subsequent downward vertical transport is
76 another vehicle for redistributing microplastics from the surface down. For example, Choy et al.
77 (2019) suggest that this mechanism, specifically, consumption by pelagic red crabs and giant
78 larvaceans, was responsible for the subsurface peaks in plastic particles concentrations observed
79 at depths near 250 m in Monterey Bay. Thus, microplastics have been found well beneath the

80 ocean surface, but less is known regarding their spatio-temporal and size/density distributions
81 (Shamskhany et al., 2021).

82 A potentially important aspect of the movement of plastics and microplastics is aggregation, a
83 process that occurs at the surface over large scales near the centers of the five major subtropical
84 gyres and has been attributed to Ekman drift, windage and inertia (Beron-Vera, 2021). Many
85 early models concentrated on the ocean surface, but Wichmann et al. (2019) has highlighted the
86 importance of resolving the full three dimensional circulation. If aggregation also occurs below
87 the surface, well beneath the direct influence of Ekman layers, the dynamics is likely to be
88 different. Indeed, modeling results by Wichmann et al. (2019), based on a framework created by
89 Lange and van Sebille (2017) and Delandmeter and van Sebille (2019), suggests that the large
90 scale accumulation associated with the garbage patches disappears below 60m depth.

91 To avoid confusion, we will refer to infinitesimal fluid elements as “fluid parcels”, and to rigid
92 plastic particles of finite size as “rigid particles”. Typically the position $x_p(t)$ of a rigid particle
93 is tracked according to

$$94 \quad x_p(t + \Delta t) = x_p(t) + \int_t^{t+\Delta t} u dt + dx_b,$$

95 where u is the fluid velocity and dx_b is an extra displacement due the non-fluid nature of the rigid
96 particle. The user can introduce custom schemes for calculating contributions to dx_b due to
97 factors such as windage and inertia (e.g. Beron-Vera et al., 2016), turbulent diffusion (e.g.
98 Kulkulka, 2012), wave induced Stokes drift (Onink et al., 2019), etc. Eulerian schemes in which
99 plastic particles are treated as concentrations, are rare, but Mountford and Morales Maqueda
100 (2019) developed an Eulerian model in which concentrations are advected by the fluid and are
101 subject to parameterized turbulence as well as sinking or rising according to a simple law

102 involving buoyancy and friction. In a similar fashion, Kvale et al. (2020) propose an Eulerian
103 model for the biological uptake and the resulting re-distribution of microplastics.

104 An alternative approach would be to use the Maxey-Riley equation (discussed below) to solve
105 for the rigid particle velocity, v , and then use the latter to compute the trajectory of that rigid
106 particle, i.e., $x_p(t + \Delta t) = x_p(t) + \int_t^{t+\Delta t} v dt$. This equation would account for the non-fluid-
107 following effects in a deductive way, however the resulting 6th-order system (for the three
108 components of velocity and position) would be computationally challenging. To better
109 understand the implications of the use of this approach while avoiding the computational burden
110 and complexity, we have elected to analyze the movement and aggregation of individual rigid
111 particles using a Maxey-Riley framework in connection with an idealized, analytically-
112 prescribed, 3D vortex flow that qualitatively resembles the geometry of the circulation in an
113 ocean eddy but is not a solution to any dynamical oceanographic equations of motion. As shown
114 by Pratt (2014) and Rypina et al. (2015), kinematic models that reproduce the correct geometry
115 are able to also reproduce the important Lagrangian features of the flow. Even in our simple
116 flow, aggregation is non-trivial, often with multiple attractors present and lack of attraction in
117 some circumstances. Thus, we wanted to thoroughly explore this simple example before
118 investigating more realistic oceanic flows. We note that other idealized studies have been carried
119 out in connection with 2D wave fields and vortex flows (e.g. DiBenedetto 2018a,b and Kelly et
120 al., 2021).

121 Aggregation can be attributed to the presence of an attractor: here, an object with a dimension
122 less than three that is somehow set up by the fluid circulation patterns and towards which rigid
123 particle trajectories attract. As long as the fluid is incompressible, fluid parcels will not
124 experience attraction and will not aggregate, but plastic particles may do so. Note also that

125 because each attractor is generally associated with its corresponding basin of attraction, if rigid
126 particles are introduced outside of the basin of attraction, they will not be attracted and will not
127 aggregate towards this attractor.

128 In order to reach a better understanding of what leads to attraction and attractors in 3D flows, we
129 explore a simple canonical example in geophysical fluid dynamics, namely the flow in a rotating
130 cylinder. This flow resembles some of the characteristics of ocean eddies, including a horizontal
131 swirl and an overturning component in the vertical, but is much less complex than any realistic
132 oceanic eddy. Specifically, we use a simple analytically-prescribed phenomenological velocity
133 introduced by Rypina et al. 2015. The Lagrangian properties of this circulation have been
134 previously studied (Fountain, et al. 2000; Pratt et al. 2014; Rypina et al. 2015) allowing us to
135 begin to investigate inertial rigid particles from an established base of knowledge. A prior theory
136 (Haller and Sapsis, 2008) governing the movement of rigid particles with high drag indicates that
137 accumulation is favored for slightly buoyant particles in flows dominated by vorticity, and this
138 also motivates our choice of background flow. Identification of the attractors that can arise in this
139 flow field, evaluating their reach and domains of attraction, and clarifying the circumstances that
140 lead to their formation are the primary objectives of this work. Although motivated by the
141 problem of marine microplastics, this study is, for now, mainly a curiosity-driven research
142 aiming to develop a basic understanding of the mechanisms that might lead to aggregation of
143 rigid particles in 3D flows. The hope is that with such basic understanding in hand, one could
144 later start investigating aggregation phenomena in more complex and more realistic ocean
145 mesoscale and submesoscale eddying flows.

146 **II. Methods**

147 The physics of the motion of a small, rigid sphere that moves with velocity $\vec{v}(t)$ through a fluid
 148 with pre-existing velocity distribution $\vec{u}(\vec{x}, t)$ has been the subject of investigation by Stokes
 149 (1851), Basset (1888), Boussinesq (1903), Faxen (1922), Oseen (1927), Tchen (1947) and many
 150 others, and was put in a unifying framework by Maxey and Riley (1983). More recent
 151 theoretical extensions include Beron-Vera et al. (2019) and Beron-Vera (2021). We will use a
 152 form of the Maxey-Riley equation that has been extended to include constant frame rotation with
 153 angular velocity $\vec{\Omega}^*$:

$$\begin{aligned}
 154 \quad \frac{d\vec{v}}{dt} = & \frac{\rho_f}{\rho_p} \frac{D\vec{u}}{Dt} + \frac{\rho_f}{2\rho_p} \left(\frac{D\vec{u}}{Dt} - \frac{d\vec{v}}{dt} \right) - \frac{9\nu\rho_f}{2\rho_p d^2} (\vec{v} - \vec{u}) + \left(1 - \frac{\rho_f}{\rho_p} \right) \vec{g} + \frac{\rho_f}{\rho_p} \vec{\Omega}^* \times (\vec{u} - \vec{v}) \\
 155 \quad & + \frac{\rho_f}{\rho_p} 2\vec{\Omega}^* \times \vec{u} - 2\vec{\Omega}^* \times \vec{v} + \left(\frac{\rho_f}{\rho_p} - 1 \right) \vec{\Omega}^* \times \vec{\Omega}^* \times \vec{x}. \tag{1}
 \end{aligned}$$

156 The frame rotation was introduced into the non-rotating Maxey-Riley equation by replacing

$$157 \quad \vec{v}_s = \vec{v}_r + \vec{\Omega} \times \vec{x}_r, \quad \vec{u}_s = \vec{u}_r + \vec{\Omega} \times \vec{x}_r,$$

$$158 \quad \frac{D_s \vec{u}_s}{Dt} = \frac{D_r \vec{u}_r}{Dt} + 2 \vec{\Omega} \times \vec{u}_r + \vec{\Omega} \times \vec{\Omega} \times \vec{x}_r, \quad \frac{d_s \vec{v}_s}{Dt} = \frac{d_r \vec{v}_r}{Dt} + 2 \vec{\Omega} \times \vec{v}_r + \vec{\Omega} \times \vec{\Omega} \times \vec{x}_r,$$

159 where subscript “s” denotes stationary frame and subscript “r” – rotating frame. Alternatively,
 160 transformation into a rotating frame can be done following the variational method of Ripa
 161 (1987). The subscripts “r” have then been dropped in Eq. (1) and all subsequent equations since
 162 all variables are now in the rotating frame. For non-spherical rigid particles, adjustments to the
 163 coefficients within the Maxey-Riley equations can be made to account for elliptical shapes (see,
 164 for example, DiBenedetto et al, 2018a,b and references therein) but at the cost of adding a third
 165 vector equation for the orientation of the ellipsoid. However, real microplastics often have

166 complex tangled-filament-like shapes which are poorly represented by an ellipsoid, and no
167 corrections for tangled filaments are currently available.

168 In Eq. (1), which is a statement of Newton's second law for the rigid particle, the right-hand side
169 represents, in order, the effects of inertia, added mass, drag, buoyancy, Coriolis acceleration
170 associated with the added mass, the Coriolis acceleration associated with the particle mass,
171 Coriolis acceleration associated with the fluid motion, and centrifugal acceleration. A similar
172 equation has been previously derived by Beron-Vera et al. (2019), though the centrifugal
173 acceleration does not appear there explicitly, having been combined with the acceleration due to
174 gravity in order to define an effective gravity and corresponding geopotential. Coordinates are
175 then imagined to be aligned with geopotential surfaces, though standard spherical or Cartesian
176 coordinates are usually used in practice (Vallis, 2006). Our explicit retention of the centrifugal
177 acceleration will later allow absolute vorticity to arise naturally as a quantity of central
178 importance. We have omitted the lift force, the Basset history force, and the Faxen corrections
179 (Gatignol, 1983). Faxen corrections account for the variation of the flow across the rigid particle
180 and are proportional to $a^2\Delta u$. For a particle size that is much smaller than the typical length scale
181 of the flow, these corrections are small and typically neglected (Haller and Sapsis, 2008; Beron-
182 Vera et al., 2019). The history term, which is an integral along a particle path, accounts for the
183 boundary layer effects that a particle leaves behind. It is typically ignored under the assumption
184 that the chances of other particles crossing that localized boundary layer before it decays are
185 small (Beron-Vera et al., 2019; see also Langlois et al., 2015 and Daitche and Tel., 2011 for
186 more info on the influence of the history term on the behavior of rigid particles). Finally, the lift
187 force arises when a particle rotates in a horizontally sheared flow. As shown in Beron-Vera
188 2019, the inclusion of the lift force leads to the next-order, $O(\tilde{\epsilon}^2)$ correction in the slow-

189 manifold approximation, and thus can also be neglected for small $\tilde{\epsilon}$. In Eq. (1), ρ_p and ρ_f are
 190 densities of the rigid particle and the fluid, d is the particle radius, ν is viscosity of the fluid, \vec{g} is
 191 the gravity vector, and $\frac{D\vec{u}}{Dt} = \frac{\partial\vec{u}}{\partial t} + \vec{u} \cdot \nabla\vec{u}$ is the fluid material derivative, evaluated for
 192 undisturbed fluid velocity at the position of the center of the rigid particle. The position $x(t)$ of a
 193 particle is determined by

$$194 \quad \frac{d\vec{x}}{dt} = \vec{v}(\vec{x}, t), \quad (2)$$

195 and together Eqs. (1) and (2) compose a coupled, 6th-order system for computation of the particle
 196 position and velocity as functions of time.

197 If the velocities and lengths are nondimensionalized using characteristic scales U and L for the
 198 background fluid flow, and L/U is used as a time scale, then Eq. (2) remains formally unchanged
 199 while the nondimensional form of Eq. (1) is

$$200 \quad \frac{d\vec{v}}{dt} = \frac{3R}{2} \frac{D\vec{u}}{Dt} + \tilde{\epsilon}^{-1}(\vec{v} - \vec{u}) + \left(1 - \frac{3R}{2}\right) \vec{g}_r + 3R\vec{\Omega} \times (\vec{u} - \vec{v}) + 2\left(\frac{3R}{2} - 1\right) \vec{\Omega} \times \vec{v}, \quad (3)$$

201 where $\tilde{\epsilon} = \frac{2\rho_f}{\rho_f + 2\rho_p}$, $\vec{g}_r = (\vec{g} - \vec{\Omega}^* \times \vec{\Omega}^* \times \vec{x}) / (L/U^2)$, $\vec{\Omega} = \frac{\vec{\Omega}^* L}{U}$ and $\tilde{\epsilon} = \frac{2}{9} \left(\frac{d}{L}\right)^2 \frac{UL}{\nu} \frac{1}{R}$ is the Stokes

202 number, the ratio of the adjustment time scale of a particle (due to drag) to the time scale of the
 203 background flow. For $\tilde{\epsilon} \ll 1$, viscous drag is the dominant force acting on the particle, implying
 204 that a particle with an initial velocity differing by an amount $> O(\tilde{\epsilon})$ from the local fluid velocity
 205 will be rapidly accelerated over a time scale $\tilde{\epsilon}$ to a velocity proximal to that of the fluid.

206 Thereafter the particle will undergo a slow evolution in which the weaker forces due to inertia,
 207 added mass, and buoyancy cause slight departures from the movement of the fluid itself.

208 The limit $\tilde{\varepsilon} \rightarrow 0$ constitutes a singular perturbation of Eq. (3), a problem that can be addressed
 209 using an approach due to Fenichel (1979) that was originally formally developed for a steady
 210 background flow, but that has been extended by Haller and Sapsis (2008) to include a time-
 211 varying background flow. In either case, it can be shown that following the initial viscous
 212 adjustment, the particle position and velocity tend toward a subspace or “slow manifold” on
 213 which the particle velocity is determined directly by the fluid velocity through an “inertial”
 214 equation, here extended to include frame rotation:

$$215 \quad \vec{v} = \vec{u} + \tilde{\varepsilon} \left(\frac{3R}{2} - 1 \right) \left[\frac{D\vec{u}}{Dt} + 2\vec{\Omega} \times \vec{u} - \vec{g}_r \right] + O(\tilde{\varepsilon}^2). \quad (4)$$

216 This result is the same as obtained by Beron-Vera et al. 2019, provided that their gravity vector
 217 is interpreted as our \vec{g}_r . The same authors also present more general cases, including those with
 218 the lift force and on the sphere. In Supplementary Material we present a simple derivation of Eq.
 219 (4) based on a multiple-scale expansion. It provides a quick, though less rigorous, alternative to
 220 the Fenichel approach.

221 A chief advantage of the slow manifold reduction is that the 6th order system given by Eqs. (2)
 222 and (3), in which particle velocity needs to be solved for, is reduced to a 3rd order system given
 223 by Eqs. (2) and (4), where the particle velocity is explicitly written as a function of fluid velocity
 224 and flow and particle parameters (and thus is known). The bracketed expression in Eq. (4), which
 225 determines the velocity of the rigid particle relative to the fluid, is nothing more than $\frac{\partial}{\partial x_j} \tau_{ij}$,
 226 where τ_{ij} is the stress tensor for the fluid. Thus the relative velocity of a rigid particle on the
 227 slow manifold is in the same direction as the net force that would act on a fluid parcel occupying
 228 the same space. Ordinarily, for a fluid parcel, that force would equate with an acceleration, but
 229 on the slow time scale, the relative particle velocity points in the same direction as the net fluid

230 force and its magnitude is proportional to $\tilde{\varepsilon} \left(\frac{3R}{2} - 1 \right) = \frac{2}{9} \frac{d^2}{L^2} \frac{UL}{\nu} \frac{(\rho_f - \rho_p)}{\rho_f}$. Since the aggregation of
 231 rigid particles requires departures of the particle velocity from the (divergence free) velocity
 232 field of the fluid, one can expect that aggregation will occur more slowly if d and $(\rho_f - \rho_p)/\rho_f$
 233 are small, or if ν is large. At the same time, the existence of attractors internal to the fluid may
 234 depend on $(\rho_f - \rho_p)/\rho_f$ being small: for example, a large density difference may mean that
 235 rigid particles simply sink to the bottom or rise to the surface (and are thus attracted to attractors
 236 external to the fluid interior).

237 As pointed out by Haller and Sapsis (2008) (also see Beron-Vera et al. 2019), we can consider a
 238 continuous concentration of rigid particles with similar properties, and with smoothly varying
 239 velocity given by Eq. (4). The aggregation of such a concentration would appear to require that
 240 the divergence of that velocity be negative (though see an apparent counterexample in Fig 1c,
 241 presented later). Following Haller and Sapsis (2008), consider the evolution of a material
 242 volume of rigid particles. The time rate of change of this volume is

$$243 \quad \frac{dV}{dt} = \oint \vec{v} \cdot \vec{n} dA_V = \iiint (\nabla \cdot \vec{v}) dV = \iiint \nabla \cdot \left[\vec{u} + \tilde{\varepsilon} \left(\frac{3R}{2} - 1 \right) \left(\frac{D\vec{u}}{Dt} + 2\vec{\Omega} \times \vec{u} - \vec{g}_r \right) \right] dV \quad (5)$$

244 where $\nabla \cdot \vec{u} = 0$ for an incompressible fluid. Shrinking V to an infinitesimal size allows the right-
 245 hand side to be approximated by V times the local value in the integrand, and the result may be
 246 integrated in time, yielding

$$247 \quad V(t) = V_0 \exp \left(\tilde{\varepsilon} \left(\frac{3R}{2} - 1 \right) \int_{t_0}^t \nabla \cdot \left(\frac{D\vec{u}}{Dt} + 2\vec{\Omega} \times \vec{u} - \vec{g}_r \right) ds \right)$$

$$248 \quad = V_0 \exp \left(-2\tilde{\varepsilon} \left(\frac{3R}{2} - 1 \right) \int_{t_0}^t [Q_r(x(s), s) + \vec{\Omega} \cdot \vec{\zeta}_r + |\vec{\Omega}|^2] ds \right)$$

249
$$= V_0 \exp\left(-2\tilde{\varepsilon} \left(\frac{3R}{2} - 1\right) \int_{t_0}^t Q_a(x(s), s) ds\right). \quad (6)$$

250 Here $Q_r = \frac{1}{2}\left(\frac{1}{2}|\vec{\zeta}_r|^2 - |S|^2\right)$ is the three-dimensional Okubo-Weiss parameter (Okubo, 1970;
 251 Weiss, 1991), $\vec{\zeta}_r$ represents the relative vorticity vector for the fluid, $S = 1/2(\nabla\vec{u} + (\nabla\vec{u})^T)$ is
 252 the strain tensor, and $|S|$ is its Frobenius norm. The final step in Eq. (6) follows from
 253 introduction of the absolute vorticity vector

254
$$\vec{\zeta}_a = \vec{\zeta}_r + \overline{2\Omega} \quad (7)$$

255 and the corresponding function $Q_a = \frac{1}{2}\left(\frac{1}{2}|\vec{\zeta}_a|^2 - |S|^2\right)$. We note that for a volume V of any
 256 size:

257
$$\frac{dV}{dt} = 2\tilde{\varepsilon} \left(\frac{3R}{2} - 1\right) \iiint Q_a dV = \tilde{\varepsilon} \left(\frac{3R}{2} - 1\right) \iiint \frac{\partial^2}{\partial x_i \partial x_j} \tau_{ij} dV = \frac{2}{9} \frac{d^2}{L^2} \frac{UL}{\nu} \frac{(\rho_f - \rho_p)}{\rho_f} \oint \frac{\partial}{\partial x_j} \tau_{ij} n_i dA_V, \quad (8)$$

259 where n_j denote the components of the outward unit vector normal to the bounding surface A_V .
 260 The first equality in Eq. (8) is a modest modification of Eq. (31) from Haller and Sapsis (2008),
 261 and one could probably have guessed that our more general result could be obtained by replacing
 262 Q with Q_a . The remainder of the equation expresses volume changes in terms of the fluid
 263 stresses. Thus for buoyant particles, a volume $V(t)$ of any size will contract if the force normal
 264 to A_V due to the fluid stresses, integrated around A_V , is inward. In many cases, including
 265 quasigeostrophic eddies and gyres, internal waves, and the surface gravity waves considered by
 266 DiBenedetto et al. (2018a,b) and all inviscid flows, the stress tensor is dominated by pressure,
 267 i.e., $\frac{\partial}{\partial x_j} \tau_{ij} \cong -\frac{1}{\rho_f} \nabla p$, so the tendency to aggregate is determined entirely by the pressure field.

268 In general, Q_a can change sign along a particle trajectory, making it hard to predict whether the
 269 surrounding volume shrinks or expands with time. If a buoyant particle is trapped in a region in
 270 which Q_a is predominately positive, then this region is a good candidate for aggregation.
 271 Persistent ocean eddies and other vortical structures are possibilities, not only because vorticity
 272 tends to dominate over strain, but also because such features have the ability to trap fluid for long
 273 periods of time. For dense particles, contraction occurs in areas dominated by strain, and it has
 274 been shown that aggregation of heavy particles can occur in strain-dominated filaments that arise
 275 in particle-laden turbulent flows, though the considered particle-to-fluid density differences tend
 276 to be quite large (see Brandt and Coletti, 2022 for a review). In our study, we will focus on
 277 vortex flows reminiscent of ocean eddies, and on lower dimension objects within such flows that
 278 can act as attractors for buoyant particles.

279 A simple example of aggregation is given by Haller and Sapsis (2006), who argue that the
 280 elliptical center of a steady, non-divergent 2d eddy, with $\vec{g} = |\vec{\Omega}|=0$, acts as an attractor for
 281 buoyant particles. Here Q_a (now $=Q_r$), is ostensibly positive near the elliptical center of the
 282 eddy, corresponding to contraction of the phase space (which in our case coincides with the
 283 physical space) of the rigid particle motion. Since the central fixed point of the velocity field of
 284 the eddy is also a fixed point of the slow manifold particle velocity (Eq. (4)), buoyant particles
 285 initiated about the center should migrate towards the center. If the eddy is inviscid and its
 286 streamlines are circular, then the pressure and azimuthal velocity are related by the cyclostrophic
 287 balance $\frac{1}{\rho_f} \frac{\partial p}{\partial r} = \frac{u_\theta^2}{r}$ so that $2Q_r = \frac{1}{\rho_f} \left(\frac{1}{r} \frac{\partial p}{\partial r} + \frac{\partial^2 p}{\partial r^2} \right)$, and for an eddy in solid body rotation ($u_\theta =$
 288 $\Gamma_s r$), $2Q_r = \frac{1}{\rho_f} \left(\frac{1}{r} \frac{\partial p}{\partial r} + \frac{\partial^2 p}{\partial r^2} \right) = 2\Gamma_s^2$. As suggested in Figure 1a, a small concentration of rigid
 289 particles indicated by the cross hatched area shrinks as it moves towards the center of the eddy.

290 The contraction is partially due to the geometric effect of movement towards smaller radius
 291 (term $\frac{1}{r} \frac{\partial p}{\partial r}$) but also due to the fact that the pressure gradient decreases to zero as the center is
 292 approached and thus the inner edge of the path moves more slowly inward than the outer part
 293 (term $\frac{\partial^2 p}{\partial r^2}$). In the case of solid body rotation the two terms contribute equally. A second
 294 example (Fig. 1b) is of an eddy with an azimuthal velocity given by $u_\theta = \Gamma_C r^{1/2}$. Here $\frac{\partial^2 p}{\partial r^2} = 0$
 295 and $2Q_r = \frac{1}{\rho_f} \left(\frac{1}{r} \frac{\partial p}{\partial r} \right) = \Gamma_C^2 / r > 0$, so the contraction of the patch is entirely due to the geometric
 296 effect of its movement towards smaller radius. The most curious case is that of a point vortex:
 297 $u_\theta = \Gamma_P r^{-1}$, for which $2Q_r = \frac{1}{\rho_f} \left(\frac{1}{r} \frac{\partial p}{\partial r} + \frac{\partial^2 p}{\partial r^2} \right) = \frac{\Gamma_P^2}{r^4} - \frac{3\Gamma_P^2}{r^4} < 0$. Here the vorticity is zero away from
 298 the eddy center and the velocity field is dominated by strain. The pressure gradient *increases* as
 299 the center of the vortex is approached, meaning that the inner part of the patch moves towards
 300 the center more rapidly than the outer portion (Fig. 1c) and this tendency (quantified by the
 301 factor $-\frac{3\Gamma_P^2}{r^4}$) surpasses the tendency towards geometrical contraction (quantified by the factor
 302 $\frac{\Gamma_P^2}{r^4}$). The area of the patch thus expands as rigid particles are drawn towards the center of the
 303 vortex. Note, however, that a patch surrounding the center of the vortex can only shrink. This
 304 behavior is made possible by the singularity at the center, and although this feature is artificial,
 305 point vortices are often used in idealized models of fluid flow and will act as sinks or “black
 306 holes” for buoyant particles even though $2Q_r < 0$.
 307 The sign of Q_a is clearly not the whole story and does not encompass the effects of boundaries.
 308 For example, consider the fate of heavy ($\rho_f < \rho_p$) particles in the eddy show in Fig. 1a. The
 309 particles will migrate outward in each case, and no interior attraction will occur unless the eddy
 310 is surrounded by a boundary, which would then act as an attractor.

311 In the next section, we will consider a more general, 3D, eddy-like circulation: one that has both
312 vertical and horizontal components of vorticity, time dependence, and a variety of vortical
313 structures that act as candidates for attraction. Our model is based on the incompressible flow in
314 a rotating cylinder (Greenspan, 1986), which has been studied in many configurations by
315 numerous authors as a model of ocean circulation (Hart and Kittelman, 1996; Pedlosky & Spall,
316 2005), ocean eddies (Pratt et al., 2014; Rypina et al., 2015), or industrial processes and
317 engineering applications (Lopez & Marques, 2010 and references therein), and can be easily set
318 up in the laboratory setting (Fountain et al., 2000; Lackey and Sotiropoulos (2006)). In its
319 original configuration the cylinder rotates about a vertical axis at a constant (positive) angular
320 velocity ($\vec{\Omega} = \Omega \vec{k}$), and the lid, which is in contact with the fluid, rotates with a slightly greater
321 angular speed. The differential rotation sets up an azimuthal circulation in the horizontal and an
322 overturning circulation in the vertical. (Overturning is observed in ocean eddies as well and
323 Ledwell et al. (2008) present an example.) The steady, axially symmetric state of the rotating
324 cylinder flow that is established will be our first object of investigation. A steady but
325 asymmetrically-perturbed variant can be established by moving the axis of rotation of the lid
326 away from the axis of rotation of the cylinder, and this offset can also be varied in order to
327 induce time dependence. Fountain et al. (2000) set a similar situation up in a laboratory cylinder
328 using a submerged impeller that can be tilted, rather than the differentially rotating lid that can be
329 shifted, to establish an asymmetric disturbance flow. The authors discussed the Lagrangian
330 characteristics of the undisturbed flow and demonstrated the existence of secondary vortical
331 structures generated when the flow is perturbed. Pratt et al. (2014) reproduced similar structures
332 using a primitive equation simulation and explored the rich assembly of chaotic regions and non-
333 chaotic vortical structures as functions of the Ekman and Rossby numbers of the flow. The time-

334 dependent version of the rotating cylinder flow and a theory describing the resulting vortical
 335 structures were discussed by Rypina et al. (2015), who based their examples on a
 336 phenomenological model that reproduced many of the qualitative features of the numerically-
 337 obtained velocity field. In dimensionless Cartesian coordinates, the model velocity field is given
 338 by

$$339 \quad u^{(x)} = -bx(1 - 2z) \frac{r_o - r}{3} - ay(c + z^2) + \varepsilon \left[y(y - y_o + \gamma \cos(\sigma t)) - \frac{r_o^2 - r^2}{2} \right] (1 - \beta z), \quad (9a)$$

$$340 \quad u^{(y)} = -by(1 - 2z) \frac{r_o - r}{3} + ax(c + z^2) - \varepsilon x(y - y_o + \gamma \cos(\sigma t))(1 - \beta z), \quad (9b)$$

$$341 \quad u^{(z)} = bz(1 - z) \frac{2r_o - 3r}{3}, \quad (9c)$$

342 in which $r = (x^2 + y^2)^{1/2}$ and r_o is the cylinder radius. The velocity field consists of a steady,
 343 axially symmetric flow of strength a with an overturning circulation of strength b . To this
 344 symmetric state one can add an asymmetric, possibly unsteady and depth dependent, perturbation
 345 of amplitude ε (not to be confused with the Stokes number $\tilde{\varepsilon}$). The perturbation is quantified by
 346 an offset parameter y_o that introduces axial asymmetry in the velocity field, a frequency σ , and
 347 an amplitude β for linear depth dependence and an amplitude γ for the time dependence. For the
 348 case of axially symmetric, steady flow ($\varepsilon = 0$) the horizontal velocity field, in cylindrical
 349 coordinates, becomes

$$350 \quad u^{(r)} = -br(1 - 2z) \frac{r_o - r}{3} \quad (10a)$$

351 and

$$352 \quad u^{(\theta)} = ar(c + z^2), \quad (10b)$$

353 where θ is the azimuthal angle. Table 1 lists the parameter values used for each numerical
354 experiment.

355 We now review the main features of the Lagrangian circulation in the rotating cylinder flow. In
356 the steady, symmetric configuration, each fluid trajectory is confined to the surface of a torus as
357 it winds around the cylinder. The typical torus is associated with quasi-periodic trajectories and
358 any such trajectory, followed for a sufficient length of time so that it completes many
359 overturning and azimuthal rotations around the cylinder, will sketch out the torus in 3D. Fig. 2b
360 contains several examples of such tori and Fig. 2a shows the corresponding Poincare map, made
361 by marking the crossing points of trajectories through a vertical slice through the cylinder. After
362 a large number of crossings each quasi-periodic trajectory traces out the cross section of the torus
363 on which it lives. The tori are nested within each another, with a single, horizontal, periodic
364 trajectory located at the center of the nest. Certain tori contain periodic trajectories, and these
365 will show up as a finite number of dots on the Poincare map. Because of this geometry, the
366 motion of fluid parcels is most naturally described in terms of action-angle-angle variables,
367 where the action, I , acts a label for a particular torus and is constant following each trajectory,
368 and the two angle variables, $\tilde{\theta}$ and ϕ , define the location of a parcel on the torus. Here $\tilde{\theta}$ is an
369 azimuthal angle that differs from the above cylindrical coordinate θ in how its origin is defined,
370 while the ‘poloidal’ angle ϕ wraps around the cross-section of each torus. The coordinates are
371 non-orthogonal but are defined in such a way that the angular velocities, $\Omega_{\tilde{\theta}}$ and Ω_{ϕ} , are also
372 constant following a trajectory. The explicit transformations to the action-angle-angle variables
373 are given in Mezic and Wiggins (1994).

374 When the symmetric RC flow is perturbed by a small, steady, symmetry-breaking perturbation,
 375 as controlled by the parameters ε and y_o in Eq. (9), the tori that are populated by periodic orbits
 376 potentially become resonant and break up, resulting in chaotic motion of fluid parcels in the
 377 vicinity (Fig. 2d-i). Tori with quasiperiodic orbits deform but stay intact. Examples are discussed
 378 by Fountain et al. (2000) and Pratt et al. (2013), and the latter found that chaos generally
 379 dominates in a large region that includes the central axis of the cylinder and extends around the
 380 boundaries of the cylinder. Away from this region the space is occupied by tori that have
 381 survived the perturbation, and these are sandwiched between tori that have broken up and created
 382 braided regions of chaos. The breakup of a torus also gives rise to new tori that appear as islands
 383 in the Poincare maps (Fig. 3d and 3g) and these contain non-chaotic trajectories. The number of
 384 islands can be predicted by a theory that decomposes the symmetry-breaking perturbation into
 385 Fourier modes, written in the $(I, \tilde{\theta}, \phi)$ coordinates, with wave numbers n and m in the $\tilde{\theta}$ and ϕ
 386 direction. If the angular velocities $\Omega_{\tilde{\theta}}$ and Ω_{ϕ} characterizing the trajectories on a particular torus
 387 satisfy the resonance condition $n\Omega_{\tilde{\theta}} + m\Omega_{\phi} = 0$ for some n and m , equivalent to the trajectories
 388 on that torus being periodic, then that torus will break up and a new set of invariant tori (islands)
 389 will form. Running through the center of the islands will be a periodic trajectory that will execute
 390 n azimuthal cycles to every m poloidal (overturning) cycles. In the case shown in Fig. 3a,
 391 $n = m = 1$, so the periodic trajectory circles the cylinder horizontally once for each overturning
 392 cycle: a so-called 1:1 resonance.

393 If the symmetry breaking perturbation is quasi-periodic in time, with underlying frequencies σ_i ,
 394 the resonance condition for the breakup of a torus becomes $n\Omega_{\tilde{\theta}} + m\Omega_{\phi} + l_i\sigma_i = 0$, where l_i 's
 395 are integers (Rypina, et al. 2015). Unlike the resonance condition for the steady perturbation,
 396 which is only satisfied on tori foliated by periodic trajectories, this new resonant condition may

397 be satisfied on tori that have quasi-periodic orbits, and the resonant islands that form will have a
398 shape and location that vary in time. An example (Fig. 2g,h) of the case of a resonance with a
399 single-frequency (i.e., time-periodic) perturbation shows a number of resonant islands. These
400 features vary in time, recovering their shape and location periodically, and the snapshots shown
401 are obtained by strobing the trajectories in 3D and at the forcing frequency. The green and blue
402 islands in Fig. 2h have resulted from the breakup of tori with quasiperiodic trajectories, and
403 center of the island corresponds to a closed material curve that is populated with quasiperiodic
404 trajectories.

405 Note that the resonance condition above and our results in general are applicable to quasi-
406 periodic disturbances with finite number of frequencies, rather than only periodic disturbances.
407 (We only show numerical simulations for the time-periodic case for simplicity.) Because any
408 broad-spectrum function can be arbitrarily closely represented by a quasi-periodic function with a
409 finite number of frequencies, this could be applicable to some oceanic flows, especially those
410 with pronounced peaks in the spectrum. However, for flows with truly broadband spectrum, this
411 approach is probably poorly applicable and/or at least impractical because of the very large
412 number of discrete frequencies needed. This is similar in its utility/applicability to other
413 Kolmogorov-Arnold-Moser—based and resonance—based arguments used in prior papers by
414 many authors (including both us and the reviewer), see, for example, Rypina et al., 2007 and
415 Beron et al., 2008; 2010.

416 **III. Results**

417 Aggregation of rigid particles will occur in presence of an attractor, an object with a dimension
418 < 3 to which particles tend asymptotically in time. We are most interested in attractors that

419 occur in the interior of the rotating cylinder, and are set up by the background circulation, as
 420 opposed to the physical boundaries of cylinder. We will see that a closed material contour
 421 consisting of periodic orbits near the core of the nested tori in the steady symmetric case act as
 422 an attractor for slightly buoyant particles, and that similar material contours consisting of
 423 periodic or quasiperiodic orbits near the centers of the resonant islands in the asymmetric cases
 424 can play the same role. We will explore three cases in increasing complexity, beginning with
 425 steady flows with axial symmetry, and proceeding to steady, asymmetric flows and finally
 426 unsteady asymmetric flows.

427 The search for attractors is motivated by the hypothesis that for cases of strong drag, where the
 428 rigid particle velocity lies close to the fluid velocity, a periodic orbit for the rigid particle motion
 429 will exist in the vicinity of a periodic trajectory for the fluid parcel motion, and that if $Q_a > 0$ in
 430 a region surrounding the latter, that it should attract buoyant particles. For the time-dependent
 431 case, we extend the search to included closed loops that contain recirculating rigid particles and
 432 that vary periodically in time.

433 (a) steady, axially-symmetric 3D flows

434 The fluid velocity field for this case is given by Eqs. (9c) and (10), and these indicate that the
 435 location of the horizontal, periodic fluid parcel trajectory living at the center of the nested tori, is
 436 given by $r = 2r_o/3$ and $z = \frac{1}{2}$. It is natural to ask whether a periodic trajectory for rigid particles
 437 also exists nearby. In the slow-manifold approximation, the steady radial, azimuthal and vertical
 438 particle velocities are obtained by writing Eq. (4) in cylindrical coordinates, leading to

$$439 \quad v^{(r)} = u^{(r)} + \tilde{\varepsilon} \left(\frac{3R}{2} - 1 \right) \left[\left(u^{(r)} \frac{\partial}{\partial r} + u^{(z)} \frac{\partial}{\partial z} \right) u^{(r)} - u^{(\theta)} \left(2\Omega + \frac{u^{(\theta)}}{r} \right) - \Omega^2 r \right] \quad (11a)$$

440
$$v^{(\theta)} = u^{(\theta)} + \tilde{\varepsilon} \left(\frac{3R}{2} - 1 \right) \left[\left(u^{(r)} \frac{\partial}{\partial r} + u^{(z)} \frac{\partial}{\partial z} \right) u^{(\theta)} + u^{(r)} \left(2\Omega + \frac{u^{(\theta)}}{r} \right) \right] \quad (11b)$$

441
$$v^{(z)} = u^{(z)} + \tilde{\varepsilon} \left(\frac{3R}{2} - 1 \right) \left[\left(u^{(r)} \frac{\partial}{\partial r} + u^{(z)} \frac{\partial}{\partial z} \right) u^{(z)} + g \right] \quad (11c)$$

442 Position of attracting periodic orbit; approximate analytical expression on a slow manifold

443 Searching for points $r = r_c$ and $z = z_c$ for which $v^{(r)} = v^{(z)} = 0$, and that lie in the proximity of

444 the horizontal trajectory of the flow, we introduce

445
$$r_c = \frac{2r_o}{3} + \tilde{\varepsilon} \left(\frac{3R}{2} - 1 \right) \tilde{r} \text{ and } z_c = \frac{1}{2} + \tilde{\varepsilon} \left(\frac{3R}{2} - 1 \right) \tilde{z}.$$

446 Substituting into the right-hand sides of (11a,c) and setting both to zero results, after neglect of

447 $O(\tilde{\varepsilon}^2)$ terms, in

448
$$r_c = \frac{2r_o}{3} + \tilde{\varepsilon} \left(\frac{3R}{2} - 1 \right) \frac{g}{b} r_o \quad (12a)$$

449 and

450
$$z_c = \frac{1}{2} + \frac{9}{2br_o} \tilde{\varepsilon} \left(\frac{3R}{2} - 1 \right) \left[\Omega^2 + a \left(c + \frac{1}{4} \right) \left(2\Omega + a \left(c + \frac{1}{4} \right) \right) \right]. \quad (12b)$$

451 For the parameters $a > 0$ and $b > 0$, circulation is cyclonic with upwelling in the center of the

452 cylinder, and $(3R/2) - 1 > 0$ for buoyant particles, so the $O(\tilde{\varepsilon})$ corrections are positive and the

453 periodic particle orbit lies at larger radius and elevation than the periodic fluid orbit. Note also

454 from Eq. (11b) that the azimuthal velocity component of the rigid particle on the periodic orbit is

455 equal to that of the fluid.

456 An explanatory sketch (Fig. 3) shows the position of the periodic orbit of the rigid particle

457 relative to that of the periodic orbit of the fluid. Since the rigid particle is buoyant, it can

458 maintain its level z only if it is situated in a region where the vertical fluid velocity is < 0 , here
 459 to the right of the fluid periodic orbit. Also, the horizontal pressure gradients associated with the
 460 centripetal acceleration associated with the frame rotation (term $\Omega^2 r$), the Coriolis acceleration
 461 (term $2\Omega u^{(\theta)}$), and the centripetal acceleration due to the azimuthal velocity $u^{(\theta)^2}/2r$ are all
 462 positive for this flow, so that low pressure exists at $r=0$ and the rigid particle is forced
 463 horizontally inward. To remain stationary the particle must sit in a region where the radial
 464 velocity of the fluid is outward. In this manner, the periodic trajectory exists at a location where
 465 the forces of inertia, buoyancy and added mass can be countered by the drag due to the
 466 background flow. If we fix all other parameters and increase Ω through positive values, the term
 467 multiplying $\tilde{\epsilon}$ in Eq. (12b) will become dominated by the Ω^2 term and will grow without bound
 468 and the periodic trajectory may cease to exist. At the same time, a periodic orbit for the rigid
 469 particle can always be found close to that of the fluid, regardless of the magnitudes of the
 470 parameters Ω , a , b etc., provided that the relative particle size d/L (and thus $\tilde{\epsilon}$), and/or the
 471 relative density difference $\frac{(\rho_f - \rho_p)}{\rho_f}$ (and thus $\frac{3R}{2} - 1$) are made sufficiently small.

472 *Position of attracting periodic orbit; conditions for the loss of periodic orbit*

473 We have suggested that periodic orbits for rigid particles are encouraged when the $\tilde{\epsilon} \left(\frac{3R}{2} - \right.$
 474 $\left. 1 \right) \ll 1$, and in the case of Run 1 the value is 0.0066. A cross-sectional plot of the radial and
 475 vertical components of the slow manifold particle velocity in a vertical section through the
 476 cylinder (Fig. 4a) shows that the periodic orbit lies at $r = 0.369$ and $z = 0.504$ (as compared to
 477 the values $r_c = 0.338$ and $z_c = 0.502$ predicted by Eq. (12). (The convergence of the
 478 surrounding velocity field is too weak to be seen in the graphic.) If $\tilde{\epsilon} \left(\frac{3R}{2} - 1 \right)$ is raised to the
 479 moderately small value 0.02, the position of periodic trajectory migrates towards larger radius

480 (Fig. 4b), the reason being that the greater buoyancy (larger value of $\frac{3R}{2} - 1$) or smaller drag
481 (larger $\tilde{\epsilon}$) requires a larger downward fluid velocity for equilibrium. Since the maximum
482 downward fluid velocity occurs at the outer cylinder wall (see Eq. (9c)) the position of the
483 periodic orbit continues to migrate outward and is lost (Fig. 4c) when $\tilde{\epsilon} \left(\frac{3R}{2} - 1 \right)$ exceeds a
484 value close to 0.3.

485 *Position of periodic orbit in numerical simulations:*

486 The slow-manifold reduction yields to the prediction (Eq. (12)) of the position of the attracting
487 material contour, or loop, for slightly buoyant particles. We can compare this prediction to what
488 is observed in numerical simulations using the Maxey-Riley Eqs. (1) and (2) over a range of
489 particle size d (and thus $\tilde{\epsilon}$) and frame rotation Ω . As shown in Fig. 5, qualitative agreement with
490 the slow-manifold prediction, and the sketch in Fig. 3, holds for a very small d (when $\tilde{\epsilon}$ is small).
491 Here the attractor in Fig. 5 is located close to the central periodic fluid parcel trajectory that lives
492 at mid-depth, $z = 0.5$ and $r = \frac{2R}{3} \approx 0.33$. As d (and $\tilde{\epsilon}$) increases, the attractor moves
493 increasingly up and outward, and although the theory captures the trends, quantitative agreement
494 with the numerical results worsens. Also, when frame rotation Ω is increased (panel c), the
495 attractor responds by shifting up from mid-depth, again in qualitative but not quantitative
496 agreement with the slow-manifold prediction in Eq. (12b).

497 *Geometry of rigid particle trajectories and evidence of attraction in numerical simulations:*

498 If in the neighborhood of the periodic rigid particle trajectory $Q_a > 0$, the phase space for
499 buoyant particles will contract and the periodic trajectory becomes a candidate for an attractor of
500 such particles. An example of the attraction towards the periodic orbit is shown in Figure 2c,
501 where a set of slightly buoyant particles ($\frac{\rho_p}{\rho_f} = 0.97$) has been initialized over the volume of the

502 cylinder, and Eqs. (1) and (2) have been integrated forward in time to determine their subsequent
503 trajectories. Each trajectory is shown using a unique color. It can be seen that the particles
504 aggregate within a ring-like structure of decreasing thickness in the general vicinity of the
505 periodic orbit of the fluid flow.

506 *Basin of attraction – relationship to Q_a :*

507 To map out the basin of attraction for the particle periodic orbit, we first consider the region over
508 which phase space contraction for the buoyant particles (i.e. $Q_a > 0$) occurs. This region is
509 shown in Fig. 6a for the current example, along with the streamlines of the fluid overturning
510 stream function. Much of the fluid flow recirculates entirely within the region of positive Q_a ,
511 whereas some of the outer streamlines cross the boundary (thick contour) between positive and
512 negative Q_a . If it were the case that rigid particles exactly followed streamlines of the fluid
513 overturning circulation, then net contraction or expansion of phase space along a rigid particle
514 trajectory would depend on the sign of the time-integrated value of Q_a along streamlines. The
515 $Q_a = 0$ contour, shown by a bold contour in each frame of Fig. 6, might then approximately
516 delineate the basin of attraction for buoyant rigid particles. In the slow-manifold approximation,
517 where rigid particle velocities lie close to the fluid velocities, the $Q_a = 0$ contour might continue
518 to do so.

519 To test this conjecture, we locate the basin of attraction in the numerical simulations by releasing
520 buoyant particles at various locations in the cross-section $0 < x < r_o$ and $0 < z < 1$, integrating
521 the subsequent trajectories over many overturning cycles, and recording the position (x_{final} and
522 z_{final}) of each particle where it crosses the same plane the final time (i.e., recording final
523 crossing with the Poincare section). We use the variable-step 4-th order Runge-Kutta integration

524 scheme, which we implemented in Matlab via the built-in function “ode45”. In our simulations, the
525 relative and absolute tolerances are set to the value of 10^{-9} to integrate particle trajectories (Eqs.
526 (2) and (3)) (our results were not sensitive to the further decrease in tolerance values). Since the
527 flow (Eqs. (9a,b,c)) is prescribed analytically and has no normal flow component at the perimeter
528 and top and bottom of the cylinder, no interpolation scheme is needed and no extra boundary
529 conditions are enforced during the integration. Integration of a trajectory is stopped when a
530 particle got within one particle radius from the cylinder walls or top/bottom. The values of z_{final}
531 as a function of initial particle position are mapped in Fig. 7a, where the large green area
532 corresponding to $z_{final} \cong 0.5$ indicates the region from which particles are attracted. Only
533 particles initiated near the central axis of the cylinder, and close to the cylinder boundaries lie
534 outside this region, and these rise to the surface of the cylinder, contact the upper lid, and are no
535 longer followed. It can be seen that the green area in Fig. 7a has an oval shape that somewhat
536 resembles the overturning streamlines at small x in the central part of the cylinder, but extends to
537 near the top, bottom and outer cylinder boundaries at larger x . Thus the $Q_a = 0$ contour provides
538 a rough indication of the size and shape of the basin of attraction, but misses some important
539 details.

540 Basin of attraction – dependence on Ω

541 We have seen that the location of the periodic orbit that acts as an attractor for buoyant particles
542 shifts up and out in response to increasing frame rotation Ω (Fig. 5c). In Fig. 8 we indicate the
543 corresponding changes in the extent of the basin of attraction with respect to changing Ω by re-
544 computing Fig. 8a with $\Omega = 0.3, 1, \text{ and } 10$. The two smaller Ω values (0.3 and 1) correspond
545 roughly to Rossby numbers $a/2\Omega$ of about 1 and 0.2, i.e., are representative of the ocean
546 submesoscale and mesoscale flows. The Q_a -functions for these cases are plotted in Fig. 6b-c.

547 Most submesoscale eddies are going to tend to have $u^{(\theta)}/r$ about the same magnitude as Ω
548 (except on the equator) and mesoscale eddies will have $u^{(\theta)}/r \ll \Omega$. The results in Fig. 8
549 suggest that, while the basin of attraction does shrink slightly with increasing Ω , this dependence
550 is weak. The main difference between the three numerical runs in Fig. 8 is in the associated
551 attraction time, which gets significantly shorter for larger values of Ω . This is explored in more
552 detail below.

553 Attraction time:

554 It follows from Eq. (6) that the attraction time towards the periodic orbit should scale as $T_a =$
555 $\left[2\tilde{\epsilon} \left(\frac{3R}{2} - 1\right) Q_a\right]^{-1}$ where $Q_a = \frac{1}{2}\left(\frac{1}{2}|\vec{\zeta}_a|^2 - |S|^2\right)$ with $\vec{\zeta}_a = \vec{\zeta}_r + \overline{2\Omega}$. Thus, for $\vec{\zeta}_r \geq 0$, as in
556 most of our numerical runs (except Experiment 1e), attraction time decreases with increasing Ω
557 for positive $\Omega \geq 0$. For negative $\vec{\zeta}_r$, which corresponds to the reversed direction of the flow in
558 our simulations (Experiment 1e), an increase in Ω will initially slow the attraction by decreasing
559 the magnitude of $\vec{\zeta}_a$ all the way to 0, at which point the periodic orbit will lose its attraction
560 properties, but then will speed up the attraction as Ω is further increased. This trend is confirmed
561 numerically in Fig. 9, where for the flow parameters corresponding to the “reversed flow” run in
562 Table 1 (Experiment 1e, with $\vec{\zeta}_r < 0$), we release a sample trajectory within the basin of
563 attraction and plot its z -coordinate as it winds around the can and eventually approaches the
564 attracting periodic orbit. As anticipated, the attraction time initially increases as Ω is increased
565 from 0 to 0.6, but then decreases as Ω is further increased to 2.

566 Disappearance of the subsurface attractor when $\tilde{\epsilon}$ becomes too large:

567 Finally, to illustrate the disappearance of the subsurface attractor when $\tilde{\epsilon}$ becomes too large, in
568 Fig. 10, we contrast 2 numerical simulations with the same flow parameters (corresponding to

569 the “slow overturn” run 1c in Table 1) but different particle diameters, $d = 10^{-3}$ vs $d = 5 \times$
570 10^{-4} . For larger d , the subsurface periodic orbit for rigid particles is no longer present within the
571 can, leading to all particles rising up to the surface (Fig. 10b). For smaller d , the periodic orbit is
572 still present and acts as an attractor for buoyant rigid particles over a significant portion of the
573 can (green region in Fig. 10a). We note that this run would be more qualitatively similar to the
574 oceanic mesoscale or submesoscale eddies, where the overturning component of circulation is
575 weak in comparison to the horizontal swirl.

576 (b) steady non-symmetrically perturbed case

577 We now consider a case in which the axial symmetry of the steady flow has been broken, here
578 through a change in the perturbation amplitude parameter ε from zero to 0.25, and in the offset
579 parameter y_0 from 0 to -0.2 in the Eqs. (9a,b). The fluid velocity field now contains something
580 like a stationary, “mode-1” azimuthal wave in the horizontal velocity field.

581 The resulting Lagrangian structure (Fig. 2d and e) has a sea of chaos that covers the near-axial
582 and outer regions of the cylinder, where no unbroken tori survive. Within this chaotic sea is a
583 region containing a nest of unbroken tori that surround a central periodic orbit. This orbit has
584 evolved from the central periodic orbit of the symmetry case and is now tilted. Within the nest of
585 unbroken tori there exist resonant layers, in which new tori have arisen, and the most prominent
586 is the “island” that is centered near $x = 0.4$ and $z = 0.2$ in the right-half (and near $x = 0.4$ and
587 $z = 0.2$ in the right half) of Fig. (2d). We further note that this center lies within the region of
588 positive Q_a (Fig. 6b). The island corresponds to the yellow tori in Fig. 3e and is produced by a
589 1:1 resonance, so that the periodic trajectory running through its center executes one complete
590 azimuthal cycle and one overturning cycle before connecting back onto itself. Thus, in this
591 steady asymmetric configuration, we now have 2 periodic orbits of the fluid flow – the central

592 slightly-tilted periodic orbit near mid-depth (that evolved from the central horizontal periodic
593 orbit of the axisymmetric flow) and a new periodic orbit running through the center of the
594 resonant island (resulting from the break-up of the resonant torus satisfying $\Omega_{\bar{\theta}} + \Omega_{\phi} = 0$).

595 We speculate that for sufficiently small $\tilde{\epsilon}$ a periodic orbit for the rigid particle motion exists in
596 the vicinity of each of the 2 periodic orbits of the fluid flow. This conjecture is difficult to prove
597 due to a complex geometry, leading to centrifugal forces that act in different directions at
598 different locations along the particle path. For now we simply search for the supposed attractors
599 by releasing particles and following their trajectories.

600 As shown in Fig. 2f, separate attractors arise in the vicinity of two periodic orbits. The first
601 appears as a ring-like structure (purple core) lying near the center of the original nested tori and
602 the second is a similar feature with a red core near the center of the resonant island. The two are
603 chained together and each has its own basin of attraction (Fig. 7c): the first consisting of a
604 roughly elliptical patch (inner green region) in the x-z-plane, which corresponds of a slice
605 through a tube-like structure in 3D, and the second consisting on an annular (blue) region that
606 surrounds the green region and that occupies a relatively larger volume.

607 In order to check that attraction of slightly-buoyant rigid particles towards periodic orbits located
608 near the centers of the resonant islands in the perturbed flow is not limited to the case of the 1: 1
609 resonance, in an additional simulation (Fig. 11, experiment 2c in Table 1), we adjusted the
610 background flow parameter b in Eqs. (9), which is responsible for the overturning strength, to
611 create a 2: 1 resonance instead of a 1: 1 resonance, as in the original run. In this case, the
612 resonant torus breaks down giving rise to a 2-island chain on the corresponding Poincare section
613 (Fig. 11a), and the fluid periodic orbit that goes through the centers of both islands completes 2

614 full cycles in azimuth and 1 complete cycle in vertical before connecting onto itself. Also, as in
615 the original run, a second slightly-tilted periodic orbit still exists near mid-depth of the can.
616 When buoyant particles are released into this flow, two attractors arise, corresponding to the 2
617 periodic orbits of rigid particles – one near mid-depth (purple core in Fig. 11c) and another in red
618 near the center of the 2: 1 resonant island.

619 *Shift in position of the periodic orbit associated with a resonant island as a function of flow and*
620 *particle parameters, and frame rotation*

621 The position of the attracting periodic orbit for rigid particles that is located within the resonant
622 islands (we will refer to it as the resonant periodic orbit) in the asymmetrically-perturbed flow
623 depends both on the perturbation strength (via ε), on the flow and particle parameters (via $\tilde{\varepsilon}$), and
624 on the frame rotation Ω . Specifically, this resonant periodic orbit for the rigid particles will shift
625 away from the corresponding periodic trajectory of the fluid flow as $\tilde{\varepsilon}$ and Ω are increased. The
626 same is true for the slightly-tilted central attracting periodic orbit near mid-depth. This is
627 qualitatively similar to the shifting of the central periodic orbit up and out from $z = 0.5$,
628 $r = 0.34$ in the axisymmetric flow in response to changing $\tilde{\varepsilon}$ and Ω , which we explored in detail
629 the previous section both analytically (Eqs. (12)) and numerically (Fig. 3-5).

630 In order to numerically illustrate the shift in the position of the attracting periodic orbits, we
631 present (Figs. 12 and 13) numerical simulations in the steady perturbed flow configuration for 3
632 values of d (and thus $\tilde{\varepsilon}$) and 3 values of Ω . As both parameters increase, the attractors move
633 away from the corresponding periodic orbits of the fluid flow. This shift is evident from the
634 change in the color of the attraction basins in (a,d,g) and from the location of the yellow cloud of
635 dots in (c,f,i) in Figs. 12-13. Increases in $\tilde{\varepsilon}$ and Ω also lead to the shrinkage of the attraction

636 basins for both attractors and to a faster convergence rate, as is evident from the tighter cloud of
637 yellow dots in (c,f,i), as discussed in more detail below. The basin of attraction for the central
638 attractor – the green region in Fig. 12 – seems to shrink faster than the basin of attraction for the
639 resonant attractor (the blue-ish region) as d increases, so when d is increased from 2×10^{-3} to
640 3×10^{-3} , the central attractor vanishes, whereas the resonant attractor is still present (Fig. 12g).
641 On the other hand, the increase in Ω (Fig. 13) causes a faster shrinkage of the basin of attraction
642 for the resonant attractor than for the central attractor, so when Ω is increased from 2 to 5 in Fig.
643 13g, the resonant attractor disappears, whereas the central attractor is still present. Figs. 12g,h,i
644 (and Fig. 13g,h,i) show cases where this threshold has been exceeded, and one of the attractors
645 has been lost, whereas the other is still present.

646 Attraction time:

647 Similar to the unperturbed flow, the attraction time for attractors in the steady, perturbed flow
648 may still scale as $T_a = \left[2\tilde{\varepsilon} \left(\frac{3R}{2} - 1 \right) Q_a \right]^{-1}$, provided that Q_a is regarded as a typical value
649 within the corresponding basin of attraction. The predicted decrease in attraction time with
650 increasing $\tilde{\varepsilon}$ and Q_a is evident from the numerical simulations in Figs. 12-13, where in (c,f,i) we
651 color-coded trajectory crossings with the x-z Poincare plain by time, with blue/yellow
652 corresponding to initial/final time. For smaller values of $\tilde{\varepsilon}$ and Ω , we observe a wider and more
653 diffuse cloud of dots (because trajectories wind around the can many times before approaching
654 the attractor), whereas as $\tilde{\varepsilon}$ and Ω increase, the clouds at comparable times become denser and
655 more compact around the attractors.

656 Basin of attraction

657 For the slightly-tilted central periodic orbit located within the central non-chaotic region near
658 mid-depth in Fig. 2f, we observe that the basin of attraction – green region in Fig. 7b – extends
659 roughly from the location of the periodic orbit to the edge of the central non-chaotic region (that
660 is foliated by discretely sampled closed curves in Fig. 2d). Note that as $\tilde{\epsilon}$ increases, the attracting
661 periodic orbit moves away from the center of this non-chaotic region towards its edge, leading to
662 the shrinkage and eventual disappearance of the corresponding basin of attraction, shown by the
663 green regions in Fig. 12a,d,g).

664 Similarly, in all of our numerical simulations, we observe that for the resonant attracting periodic
665 orbit running through the resonant islands, the basin of attraction seems to cover the region
666 between the orbit and the edge of the corresponding resonant island. An analytical expression for
667 the width of the (non-degenerate) resonant island in the fluid flow (Pratt et al., 2014) predicts

668 that $\Delta I = \sqrt{\frac{\epsilon F_{nm}^0(I_0)}{\left(n \frac{d^j \Omega_\phi}{dI^j} + m \frac{d^j \Omega_\theta}{dI^j}\right)_{I_0}}}$, where ΔI is the deviation in the action coordinate away from I_0 , the

669 value of action at the resonant torus (i.e., at the center of the island). This width depends on the
670 strength of the perturbation ϵ , the order of the resonance (via n and m in the resonance

671 condition), the background flow (via $\frac{d^j \Omega_\phi / \theta_j}{dI^j}$), and the structure of the perturbation (via $F_{nm}^0(I_0)$).

672 This expression could be used as an upper limit on the extent of the basin of attraction. However,
673 because the attracting periodic orbit will move away from the center of the island towards its
674 edge as $\tilde{\epsilon}$ and Ω increase, the basin of attraction for the resonant attractor (blue region in Figs.
675 12a,d and 13a,d) becomes increasingly smaller than ΔI . One might speculate, then, that the
676 attractor will completely disappear when the attracting periodic orbit reaches the edge of the
677 resonant island. This is the case in Figs. 13g where the resonant attractor is no longer present.

678 (c) non-steady, non-symmetrically perturbed case

679 The final case that we will consider is one in which the perturbation is asymmetric and varies
680 periodically in time. The chosen perturbation frequency, $\sigma = 2\pi/9.1$, causes 2 strong additional
681 resonances (compared to the steady perturbed case) – one with $n = 0$, $m = 1$, and $l = 1$ (i.e.,
682 with a torus whose overturning frequency is equal to the perturbation frequency) that is shown in
683 blue in Fig. 2g,h and is located near the outer edge of the central non-chaotic region, and another
684 resonance, shown in green in Fig. 2g,h, with $n = 1$, $m = 1$, and $l = 1$, which is located between
685 the central non-chaotic region and the larger $n = 1$, $m = 1$ resonant island (that was present in
686 the steady case as well). Both of these new resonant structures are time dependent, their shape
687 and position recurring periodically. For example, the blue island, which looks like a crescent
688 moon pointing upward on the Poincare section at $t = 0$, becomes a crescent moon pointing
689 downward at time 4.55. The movement of the green island is more complex, as it turns both in
690 azimuth and vertical, making one complete loop over 9.1 time units. Because of the time-
691 dependence, trajectories must be strobed at the forcing frequency σ in order to capture
692 ‘snapshots’ of their forms as they recur at a particular phase in the time cycle. At the center of
693 each feature is a closed material curve that also varies periodically. Where the island has
694 emerged from the breakup of a torus with quasiperiodic orbits, the individual trajectories that
695 populate the material curves are themselves quasiperiodic.

696 Particle trajectory computations in this case confirm that the purple, red and green islands give
697 rise to attractors (Fig. 3i), whereas the blue island does not. In fact, slightly-buoyant rigid
698 particles that are released in the blue region converge towards the attractor that lies near the
699 purple region. This is also indicated by the basin of attraction of the central attractor extending
700 across the space occupied by the blue resonant island in Fig. 7c.

701 **IV. Discussion**

702 We have considered attraction phenomena for small, finite size, spherical, buoyant, rigid
703 particles in a three-dimensional rotating cylinder flow with azimuthal rotation and overturning,
704 and both with or without time dependence. The aim has been to gain insights into the behavior of
705 slightly buoyant microplastic particles in 3D vortex flows that qualitatively resemble ocean
706 eddies. The rigid particle motion is governed by a simplified version of the Maxey-Riley
707 equations (accounting for inertia, buoyancy and simplified quantification of drag and added
708 mass), and, approximately, by the slow-manifold reduction of these equations. We have
709 illustrated the possibility of aggregation of slightly-buoyant rigid particles in 3D vortex flows
710 towards closed loop attractors located subsurface within the interior of the flow. Even in our
711 idealized flow and for spherical particles with fixed radius and buoyancy, aggregation is non-
712 trivial, often with multiple attractors present and/or the lack of attraction in some circumstances.

713 Our rotating cylinder model is much less complex than any real ocean eddy in many respects,
714 including the assumed quasiperiodic time dependence and the absence of decay and interaction
715 with the surroundings. Understanding aggregation in a simple periodic flow seems like a
716 reasonable first step towards understanding aperiodic, interacting, and decaying oceanic eddies.

717 This approach is common in applications of dynamical systems theory to oceanography and
718 meteorology. For example, arguments relating to the increased stability of jets due to the strong
719 Kolmogorov-Arnold-Moser stability near shearless trajectories have first been developed for
720 spatially-periodic and time-quasiperiodic flows and tested using idealized toy models, before
721 exploring these ideas in more realistic oceanic and atmospheric settings (see Rypina et al., 2007
722 and Beron et al., 2008; 2010). Note also that our results are applicable to quasi-periodic
723 disturbances with finite number of frequencies rather than just periodic disturbances (we only

724 show numerical simulations for the time-periodic case for simplicity), and a quasiperiodic
725 function might potentially be useful for approximating temporal variability in some oceanic
726 flows, especially those with pronounced peaks in the spectrum.

727 We have explored a steady axisymmetric rotating cylinder flow and a steady flow with its axial
728 symmetry broken. In all cases, we have observed emergence of subsurface attracting structures
729 that lead to the aggregation of buoyant particles towards them. We have linked these attractors to
730 the periodic orbits of rigid particles that exist in a region of net contraction of the phase space of
731 the particle motion. The slow manifold equations suggest that periodic orbits for rigid particles
732 exist near periodic orbits of the underlying fluid flow, provided the drag is sufficiently strong
733 (Stokes number $\ll 1$).

734 We have also explored one case of an axially asymmetric and time-periodic flow, with focus on
735 the resonant “islands” that arise due to the time-dependence. At the center of such islands are
736 closed material contours, or loops, composed of quasi-periodic orbits of the fluid flow. One such
737 structure has a nearby attractor, also a closed loop of quasiperiodic orbits for rigid particles,
738 while a second example does not. A detailed explanation awaits formulation of a quantitative
739 theory, something that is beyond the scope of the present paper and that will be presented in a
740 future work.

741 We have observed that the disappearance of an attractor, which can occur as the result of
742 increasing rigid particle size or frame rotation, coincides roughly with the displacement of the
743 position of the attractor to the outer edge of the resonant island from which it sprang. Whether
744 this purely geometric observation forms the basis for a general criterion for the loss of attraction
745 is unknown, as a dynamical justification is needed.

746 Marine microplastics can have complex non-spherical tangled-filament shapes, change their
747 physical and chemical properties in time due to aging and photo- or chemical-decay processes
748 (Andrady 2011), are subject to biofouling (see recent relevant work by Kreczak et al., 2021), and
749 may interact leading to the formation of clusters. None of these effects were considered in this
750 paper, and all will need to be taken into account for the realistic prediction of marine
751 microplastic evolution and re-distribution in the ocean. Real ocean eddies are also decaying in
752 time and are usually moving (translating) rather than stationary. Translation with a constant
753 velocity can be handled by considering the flow in a moving frame of reference, but decay and
754 interactions will likely change the geometry of the circulation and make the flow truly aperiodic.
755 Our simplified model cannot account for these effects, which will need to be explored separately
756 later.

757 **Acknowledgements:** Work supported by the NSF grant OCE# 2124210 and ONR CALYPSO
758 grants #N000141812417 and #N000141812165.

759 **Data Availability Statement:** No observational data was used. Details of the numerical
760 simulations using an analytical vortex model are provided in text.

761 **Author Contribution Statement:** IR led the overall effort and performed most of the numerical
762 simulations, LP contributed towards the theoretical understanding and interpretation of the
763 results, MD participated in the overall effort.

764 **Competing interests Statement:** no competing interests

765

766

767 **References**

- 768 Andrady, A.L., 2011. Microplastics in the marine environment. *Marine pollution bulletin*, 62(8),
769 pp.1596-1605.
- 770 Basset, A. B. (1988). Treatise on Hydrodynamics, Deighton Bell, London, Vol. 2, Chap. 22, pp.
771 285-297.
- 772 Beron-Vera, F. J., M. G. Brown, M. J. Olascoaga, I. I. Rypina, H. Kocak, and I. A.
773 Udovydchenkov (2008). Zonal jets as transport barriers in planetary atmospheres. *Journal of*
774 *Atmospheric Science*, 65, 3316-3326.
- 775 Beron-Vera, F. J., M. J. Olascoaga, M. G. Brown, H. Kocak, and I. I. Rypina (2010). Invariant-
776 tori-like Lagrangian coherent structures in geophysical flows. *Chaos*, 20, 017514,
777 doi:10.1063/1.3271342.
- 778 Beron-Vera, F. J., M. J. Olascoaga and R. Lumpkin, 2016. Inertia-induced accumulation of
779 flotsam in the subtropical gyres. *Geophys. Res. Lett.*, 43, 12228-12233,
780 <https://doi.org/10.1002/2016g1071443>.
- 781 Beron-Vera, F. J., M. J. Olascoaga and P. Miron, 2019. Building a Maxey-Riley framework for
782 surface ocean inertial particle dynamics. *Phys. Fluids* 31; doi: 10.1063/1.5110731.
- 783 Beron-Vera, F.J., 2021. Nonlinear dynamics of inertial particles in the ocean: From drifters and
784 floats to marine debris and Sargassum. *Nonlinear dynamics*, 103(1), pp.1-26.
- 785 Boussinesq, J. (1903) *Theorie Analytique de la Chaleur*, L'Ecole Polytechnique, Paris, Vol.2, p.
786 224.

787 Brandt, L. and F. Coletti (2022) Particle-Laden Turbulence: Progress and Perspectives. Ann.
788 Rev. Fluid Mich. 54, 159-189. <https://doi.org/10.1146/annurev-fluid-030121-021103>

789 Choy, C.A., Robison, B.H., Gagne, T.O., Erwin, B., Firl, E., Halden, R.U., Hamilton, J.A.,
790 Katija, K., Lisin, S.E., Rolsky, C. and S. Van Houtan, K., 2019. The vertical distribution and
791 biological transport of marine microplastics across the epipelagic and mesopelagic water
792 column. *Scientific reports*, 9(1), p.7843.

793 Daitche, A. and Tél, T., 2011. Memory effects are relevant for chaotic advection of inertial
794 particles. *Physical review letters*, 107(24), p.244501.

795 Delandmeter, P. and E. van Sebille (2019). The Parcels v2.0 Lagrangian framework: new field
796 interpolation schemes. *Geosci. Model Dev. Discuss.*, <https://doi.org/10.5194/gmd-2018-339>

797 DiBenedetto, M. H., N. T. Ouellette, and J. R. Koseff, 2018a. Transport of anisotropic particles
798 under waves. *J. Fluid. Mech.* 837, 320-340, doi:10.1017/jfm.2017.853.

799 DiBenedetto, M.H. and Ouellette, N.T., 2018b. Preferential orientation of spheroidal particles in
800 wavy flow. *Journal of Fluid Mechanics*, 856, pp.850-869.

801 Faxén, H., 1922. Der Widerstand gegen die Bewegung einer starren Kugel in einer zähen
802 Flüssigkeit, die zwischen zwei parallelen ebenen Wänden eingeschlossen ist. *Annalen der*
803 *Physik*, 373(10), pp.89-119.

804 Fountain, G.O., Khakhar, D.V., Mezić, I. and Ottino, J.M., 2000. Chaotic mixing in a bounded
805 three-dimensional flow. *Journal of Fluid Mechanics*, 417, pp.265-301.

806 Froyland, G., Stuart, R. M., & van Sebille, E. (2014). How well-connected is the surface of the
807 global ocean?. *Chaos*, 24(3), 033126. <https://doi.org/10.1063/1.4892530>

808 Fenichel, N.: Geometric singular perturbation theory for ordinary differential equations. *J. Differ.*
809 *Equ.* 31, 51–98 (1979)

810 Gatignol, R., 1983. The Faxén formulae for a rigid particle in an unsteady non-uniform Stokes
811 flow.

812 Greenspan, H. P., 1968. *The theory of rotating fluids* (Vol. 327). Cambridge: Cambridge
813 University Press.

814 Haller, G., and T. Sapsis, 2008. Where do inertial particles go in fluid flows? *Physica D*, 237,
815 573-583.

816 Hart, J.E. and Kittelman, S., 1996. Instabilities of the sidewall boundary layer in a differentially
817 driven rotating cylinder. *Physics of Fluids*, 8(3), pp.692-696.

818 Kelly, R., D. B. Goldstein, S. Suryanarayanan, M. B. Torielli and R. A. Handler, The nature of
819 bubble entrapment in a Lamb-Oseen vortex. *Phys. Fluids* 33, 061702;
820 <https://doi.org/10.1063/5.0053658>.

821 Kooi, M., Reisser, J., Slat, B., Ferrari, F.F., Schmid, M.S., Cunsolo, S., Brambini, R., Noble, K.,
822 Sirks, L.A., Linders, T.E. and Schoeneich-Argent, R.I., 2016. The effect of particle properties
823 on the depth profile of buoyant plastics in the ocean. *Scientific reports*, 6(1), p.33882.

824 Kreczak, H., Willmott, A.J. and Baggaley, A.W., 2021. Subsurface dynamics of buoyant
825 microplastics subject to algal biofouling. *Limnology and Oceanography*, 66(9), pp.3287-
826 3299.

827 Kukulka, T., Proskurowski, G., Morét-Ferguson, S., Meyer, D. W., & Law, K. L.(2012). The
828 effect of wind mixing on the vertical distribution of buoyant plastic debris. *Geophysical*

829 *Research Letters*, 39, L07601. <https://doi.org/10.1029/2012GL051116>

830 Kvale, K., Prowe, A.F., Chien, C.T., Landolfi, A. and Oschlies, A., 2020. The global biological
831 microplastic particle sink. *Scientific reports*, 10(1), p.16670.

832 Lackey, T.C. and Sotiropoulos, F., 2006. Relationship between stirring rate and Reynolds
833 number in the chaotically advected steady flow in a container with exactly counter-rotating
834 lids. *Physics of Fluids*, 18(5).

835 Landrigan PJ, Raps H, Cropper M, Bald C, Brunner M, Canonizado EM, Charles D, Chiles TC,
836 Donohue MJ, Enck J, Fenichel P, Fleming LE, Ferrier-Pages C, Fordham, R, Gozt A, Griffin
837 C, Hahn ME, Haryanto B, Hixson R, Ianelli H, James BD, Kumar P, Laborde A, Law KL,
838 Martin K, Mu J, Mulders Y, Mustapha A, Niu J, Pahl S, Park Y, Pedrotti M-L, Pitt JA,
839 Ruchirawat M, Seewoo BJ, Spring M, Stegeman JJ, Suk W, Symeonides C, Takada H,
840 Thompson RC, Vicini A, Wang Z, Whitman E, Wirth D, Wolff M, Yousuf AK, Dunlop S.
841 The Minderoo-Monaco Commission on Plastics and Human Health. *Annals of Global
842 Health*. 2023; 89(1): 23, 1–215. DOI: <https://doi.org/10.5334/aogh.4056>

843 Lange, M. and E. van Sebille (2017) Parcels v0.9: prototyping a Lagrangian ocean analysis
844 framework for the petascale age. *Geosci. Model Dev.*, 10, 4175-4186.
845 <https://doi.org/10.5194/gmd-10-4175-2017>

846 Langlois, G.P., Farazmand, M. and Haller, G., 2015. Asymptotic dynamics of inertial particles
847 with memory. *Journal of nonlinear science*, 25, pp.1225-1255.

848 Ledwell, J. R., McGillicuddy, D. J., and Anderson, L. A., “Nutrient flux into an intense deep
849 chlorophyll layer in a mode-water eddy,” *Deep Sea Res., Part II* 55, 1139–1160 (2008).

850 Maxey, M.R. and J. J. Riley, 1983. Equation of motion for a small rigid sphere in a nonuniform
851 flow. *Phys. Fluids* 26, 883.

852 Mountford, A. S. and M. A. Morales Maqueda (2019) Eulerian Modeling of the
853 Three-Dimensional Distribution of Seven Popular Microplastic Types in the Global Ocean.
854 *J. Geophys. Res.: Ocean*, 124, 8558-8573. [https://doi:10.1029/2019JC015050](https://doi.org/10.1029/2019JC015050).

855 Onink, V., Wichmann, D., Delandmeter, P., and van Sebille, E., 2019: The role of Ekman
856 currents, geostrophy and Stokes drift in the accumulation of floating microplastic, *Journal of*
857 *Geophysical Research: Oceans*, 124, 1474-1490, <https://doi.org/10.1029/2018JC014547>,

858 Okubo, A., 1970, June. Horizontal dispersion of floatable particles in the vicinity of velocity
859 singularities such as convergences. In *Deep sea research and oceanographic abstracts* (Vol.
860 17, No. 3, pp. 445-454). Elsevier.

861 Pabortsava, K. and Lampitt, R.S., 2020. High concentrations of plastic hidden beneath the
862 surface of the Atlantic Ocean. *Nature communications*, 11(1), p.4073.

863 Pedlosky, J. and Spall, M.A., 2005. Boundary intensification of vertical velocity in a β -plane
864 basin. *Journal of physical oceanography*, 35(12), pp.2487-2500.

865 Pratt, L. J., I. I. Rypina, T. Özgökmen, H. Childs, and T. Bebieva, 2014. Chaotic Advection in a
866 Steady, 3D, Ekman-Driven Circulation. *J. Fluid Mech*, 738, 143-183,
867 DOI:10.1017/jfm.2013.583.

868 Ripa, P., 1987. On the stability of elliptical vortex solutions of the shallow-water
869 equations. *Journal of Fluid Mechanics*, 183, pp.343-363.

870 Rypina, I. I., M. G. Brown, F. J. Beron-Vera, H. Kocak, M. J. Olascoaga, and I. A.

871 Udovydchenkov (2007). Robust transport barriers resulting from strong Kolmogorov-
872 Arnold-Moser stability. *Physical Review Letters*, 98, 104102,
873 doi:10.1103/PhysRevLett.98.104102.

874 Rypina, I. I., L. J. Pratt, P. Wang, T. M. Ozgokmen, and I. Mezić, 2015. Resonance phenomena
875 in a time-dependent, three-dimensional, Ekman-driven eddy. *J. Chaos.*, 25, 087401,
876 <http://dx.doi.org/10.1063/1.4916086>.

877 Shamskhany, A., Z. Li, P. Patel and S. Karimpour, 2021. Evidence of Microplastic Size Impact
878 on Mobility and Transport in the Marine Environment: A Review and Synthesis of Recent
879 Research. *Front. Mar. Sci.* 8:760649. Doi: 10.3389/fmars.2021.760649.

880 Stokes, G. G. (1851) *Trans. Camb. Phil. Soc.* 9, 8. (*Mathematical and Physical Papers* 3,1.)

881 Tchen, C. M. (1947). Ph. D. thesis, Delft, Martinus Nijhoff, The Hague/

882 van Sebille E., C. Wilcox, L. Lebreton, N. Maximenko, B.D. Hardesty, J.A. van Franeker, M.
883 Eriksen, D. Siegel, F. Galgani, K.L. Law (2015) A global inventory of small floating plastic
884 debris *Environ. Res. Lett.*, 10 (2015), p. 124006, 10.1088/1748-9326/10/12/124006

885 Wichmann, D., P. Delandmeter and E. van Sebille, 2019. Influence of Near-Surface Currents on
886 the Global Dispersal of Marine Microplastics. *J. Geophys. Res. (Oceans)*, 124(8),
887 <https://doi.org/10.1029/2019JC015328>

888 Weiss, J., 1991. The dynamics of enstrophy transfer in two-dimensional hydrodynamics. *Physica*
889 *D: Nonlinear Phenomena*, 48(2-3), pp.273-294.

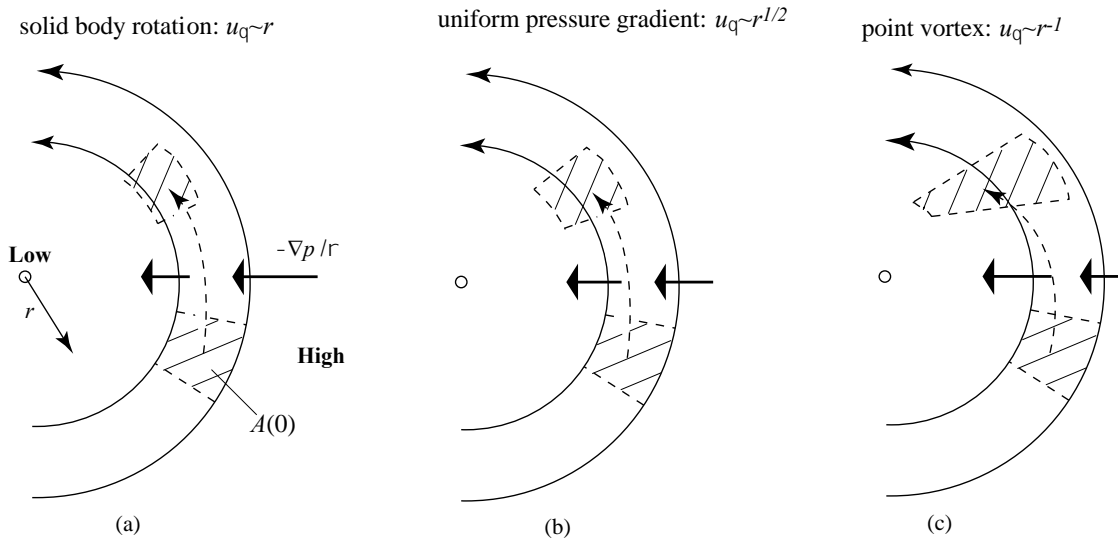
890

Experiment	a	b	ε	y_o	σ	γ	β	Ω	d
1 – steady symmetric	0.62	7.5	0	0	0	0	0	0	10^{-3}
1a (small Ω)	0.62	7.5	0	0	0	0	0	0.3	10^{-3}
1b (large Ω)	0.62	7.5	0	0	0	0	0	1	10^{-3}
1c (slow overturn)	0.62	0.25	0	0	0	0	0	1	10^{-3} vs. 5×10^{-4}
1d ($z_{attractor}$ vs Ω)	0.62	7.5	0	0	0	0	0	Sweep 0 to 10	10^{-3}
1e (reversed flow)	-0.62	-7.5	0	0	0	0	0	0, 0.6, 2	10^{-3}
2 – steady asymmetric	0.62	7.5	0.25	-0.2	0	0	0	0	10^{-3}
2a (small Ω)	0.62	7.5	0.25	-0.2	0	0	0	0.3	10^{-3}
2b (large Ω)	0.62	7.5	0.25	-0.2	0	0	0	1	10^{-3}
2c (2:1 resonance)	0.62	3.8	0.25	-0.2	0	0	0	0	10^{-3}
3 - non-steady asymmetric	0.62	7.5	0.25	-0.2	$\frac{2\pi}{9.1}$	0.2	1	0	10^{-3}

891 Table 1: Dimensionless parameter values for numerical experiments. Fixed parameters in the
892 kinematic model (Eqs. 9a-c) are $c = 0.69$, and $r_0 = 1/2$ in all cases. Parameters that appear in
893 the nondimensional Maxey-Riley Eq. (3) are also nondimensional, with L , U , L/U as length,
894 velocity and time scales. Fixed parameter values based on $L = 1\text{m}$ and $U = 1\text{m/s}$ include

895 $\frac{\rho_p}{\rho_f} = 0.97$, $R = \frac{2\rho_f}{\rho_f + 2\rho_p} = 0.680$, $\frac{3R}{2} - 1 = .020$ $\vec{g}_r = \frac{gL}{U^2} = 10.0$, $\tilde{\varepsilon} = \frac{2}{9} \left(\frac{d}{L}\right)^2 \frac{UL}{\nu R} = 0.33$, and

896 $\tilde{\varepsilon} \left(\frac{3R}{2} - 1\right) = 0.0067$. Note that $\vec{\Omega} = \Omega \vec{k} = \frac{\vec{\Omega}^* L}{U}$.



897

898 Figure 1. Three types of two-dimensional eddies with zero frame rotation and for which gravity
 899 is imagined to be zero: solid body rotation (a), constant pressure gradient (b), and point vortex
 900 (c). In each case, the cross hatched area represents a concentration of rigid particles with area
 901 $A(t)$.

902

903

904

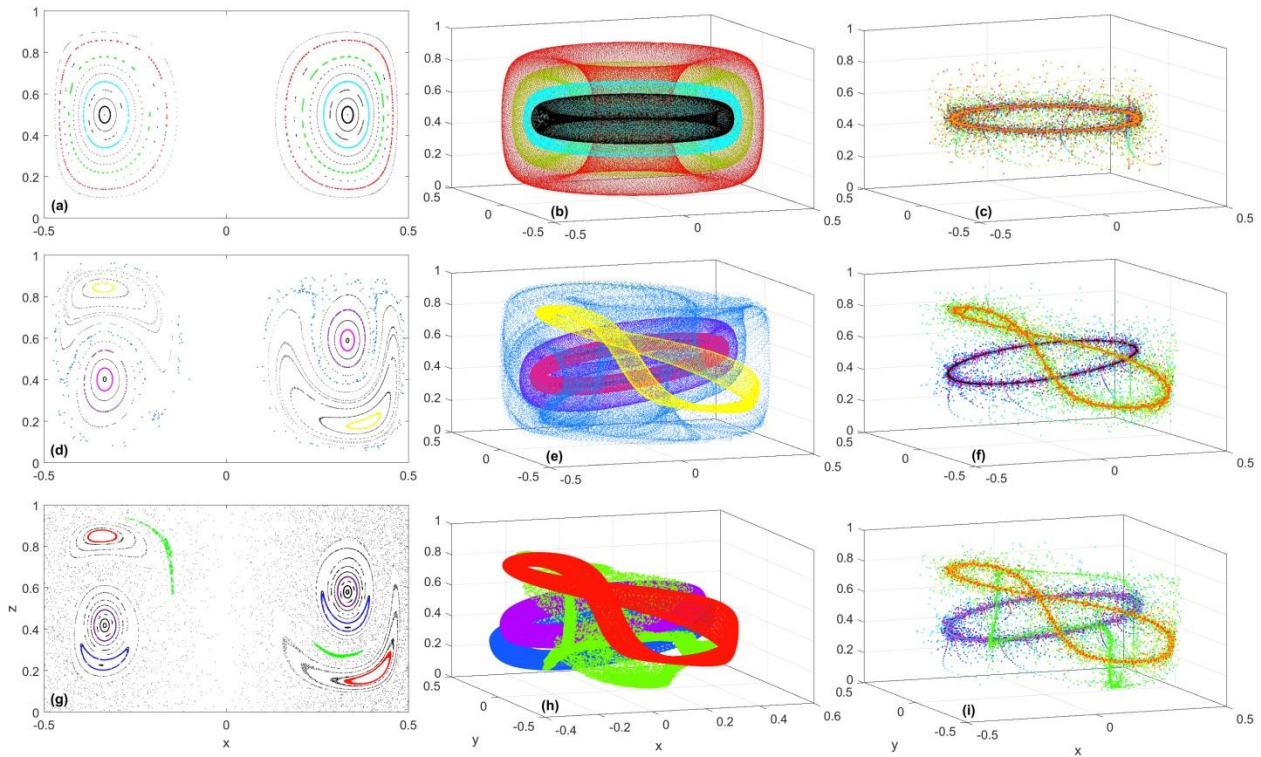
905

906

907

908

909



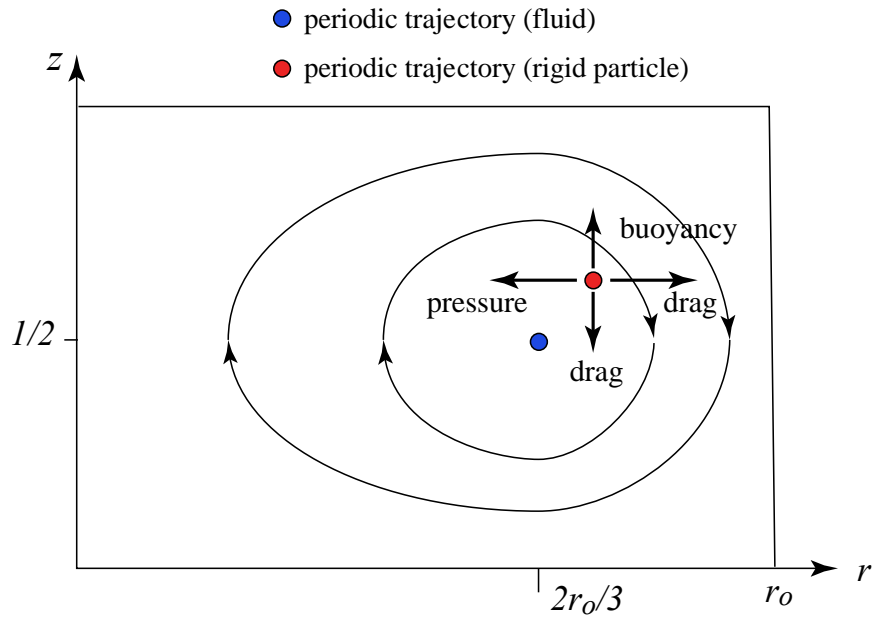
910

911 Figure 2. (left) Poincaré section, (middle) fluid parcels trajectories in 3D, (right) buoyant particle
 912 trajectories in 3D for a steady symmetric fluid flow (top row), steady asymmetric flow (middle
 913 row), and non-steady, asymmetric flow. Parameter setting are listed under Experiments 1, 2 and
 914 3 in Table 1. Colors in the left column of panels match the corresponding panel in the middle
 915 column, but the colors in the right column indicated time after release of the particles. Note the
 916 attraction of buoyant particles to a single attractor at mid-depth in panel (c), to 2 attractors in
 917 panel (f), and to 3 attractors in panel (i). Particles are released along a vertical line $x = 0.334$,
 918 $y = 0$, $0 < z \leq 0.6$ with initial velocity equal to that of the co-located fluid parcels.

919

920

921



922

923 Figure 3. Sketch showing the position in a vertical section of the periodic orbit (red dot) of the
 924 rigid particle relative to the periodic orbit (blue dot) of the fluid flow. The viewer sees one half
 925 of a vertical slide through the cylinder, with the azimuthal flow directed away from the viewer
 926 and the cylinder center at the left edge.

927

928

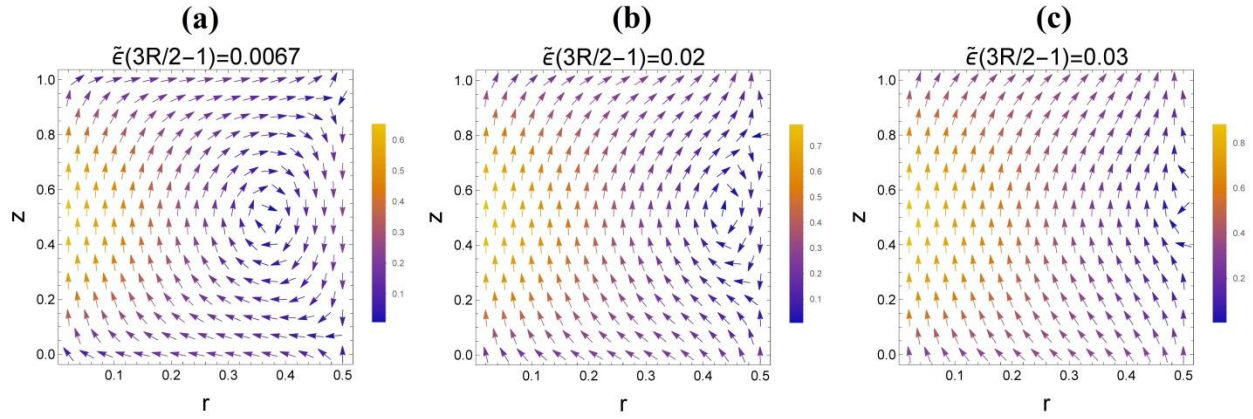
929

930

931

932

933



934

935 Figure 4. The slow-manifold radial and vertical velocity components for the rigid particles,

936 plotted in the (r, z) plane for (a) $\tilde{\varepsilon} \left(\frac{3R}{2} - 1 \right) = 0.0067$, (b) = 0.02, and (c) = 0.03. Other

937 parameters are as listed for Experiment 1a in Table 1.

938

939

940

941

942

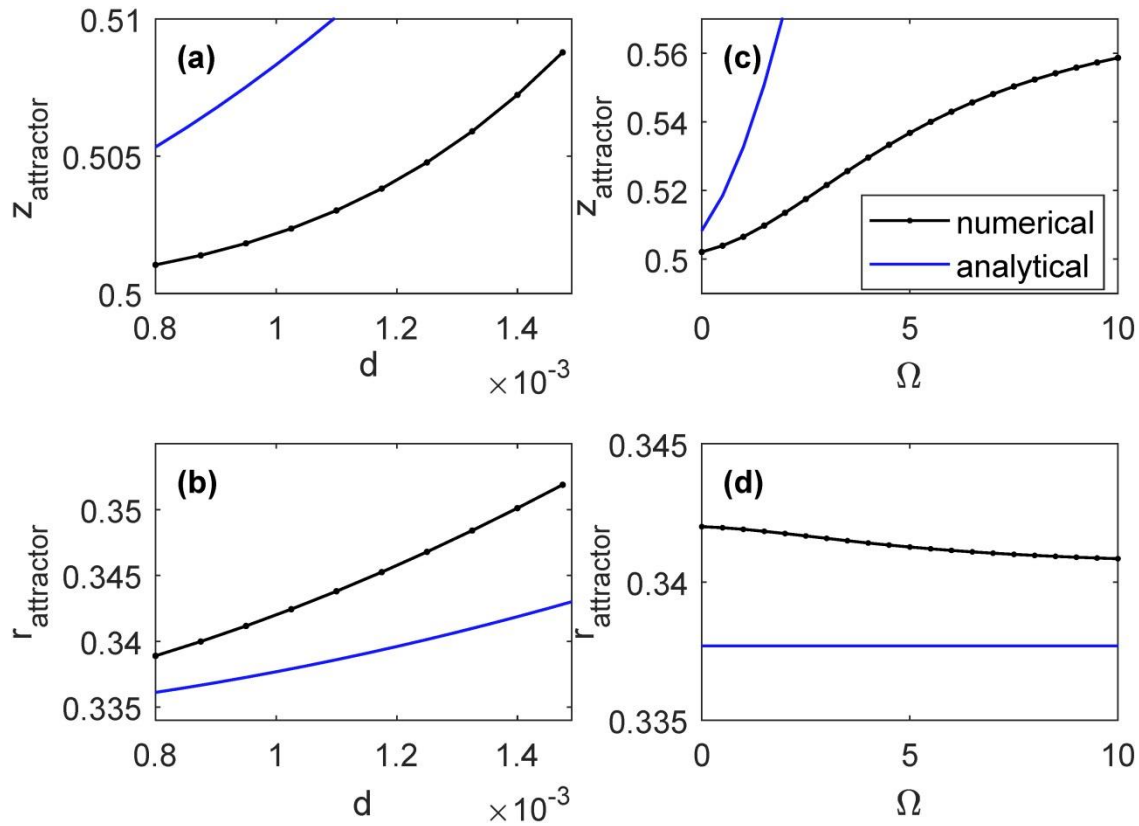
943

944

945

946

947



948

949 Figure 5. For the steady symmetric rotating cylinder flow, the coordinates of the periodic orbit
 950 that acts as an attractor for buoyant particles as a function of particle diameter (a-b) and frame
 951 rotation (c). Flow parameters are listed in Table 1 and correspond to Experiment 1 for (a-b) and
 952 Experiment 1d for (c-d).

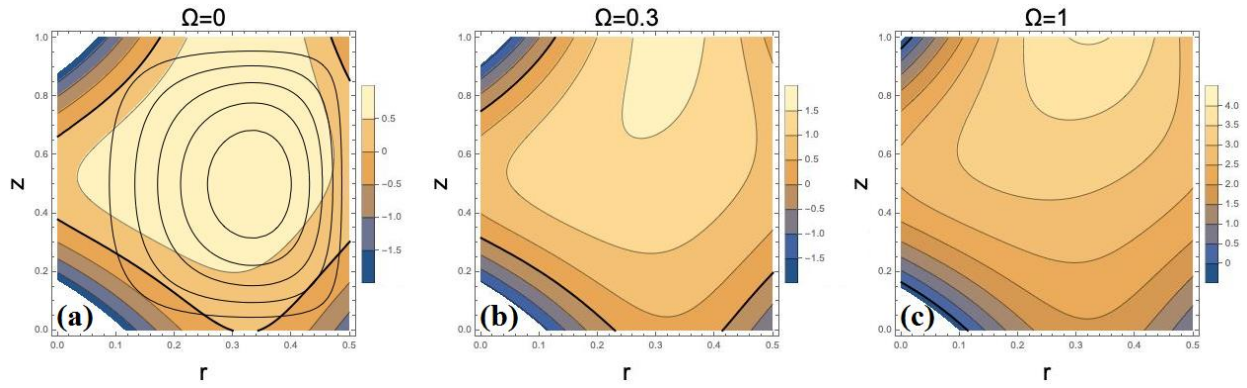
953

954

955

956

957



958

959 Figure 6. (a): The Q_a function for the steady, axisymmetric, cylinder flow with the same
 960 parameter setting (see Experiment 1a) as for Figure 3a-c, and plotted in (x,z) along with the
 961 streamlines of the overturning circulation. The thick rigid curve corresponds to $Q_a = 0$. (b): The
 962 same parameter settings, except Ω has been raised from 0 to 0.3 (Rossby number $\cong 1$) (c):
 963 $\Omega = 1.0$. (Rossby number $\cong 0.2$).

964

965

966

967

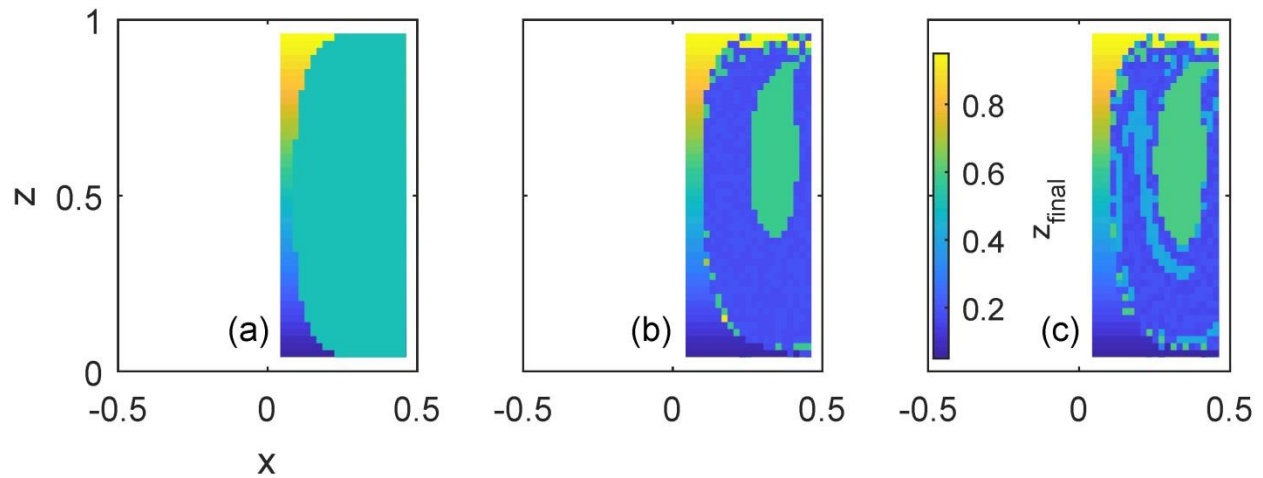
968

969

970

971

972



973

974 Figure 7. Domain of attraction for the attractors in (a) steady symmetric (Experiment 1 in Table
 975 1), (b) steady asymmetric (Experiment 2 in Table 1), and (c) time-periodic asymmetric rotating
 976 cylinder flow (Experiment 3 in Table 1). (These are the same 3 experiments that were used to
 977 produce Fig. 2.) The color indicates the height (i.e., value of z-coordinate) of the final crossing of
 978 a trajectory with the Poincare section, as a function of particle's release location. Particles
 979 attracted to the same attractor thus correspond to same color.

980

981

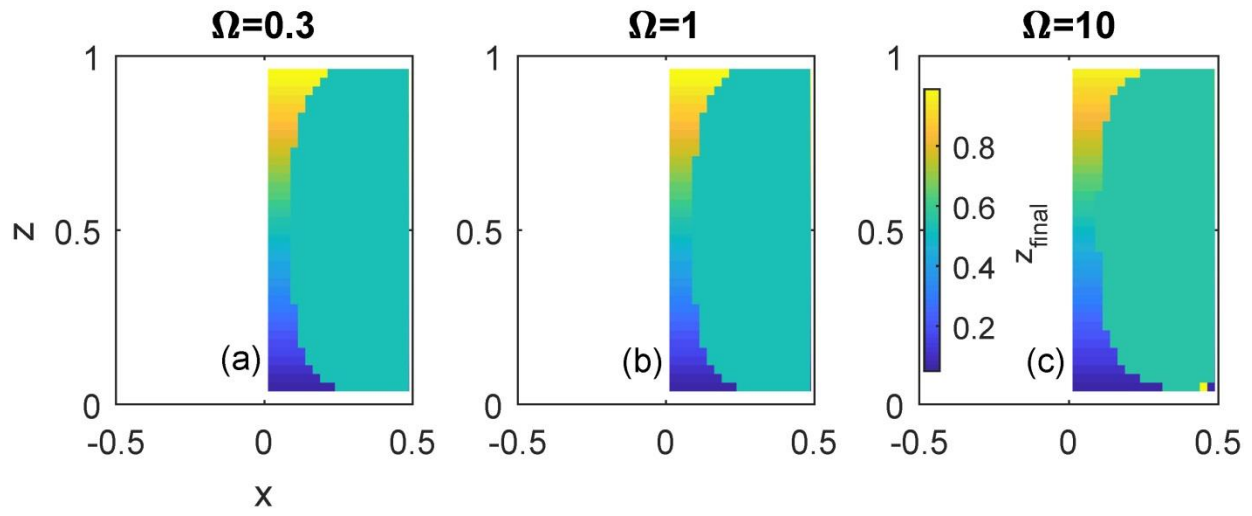
982

983

984

985

986



987

988 Figure 8. Same as in Fig. 7a but with frame rotation.

989

990

991

992

993

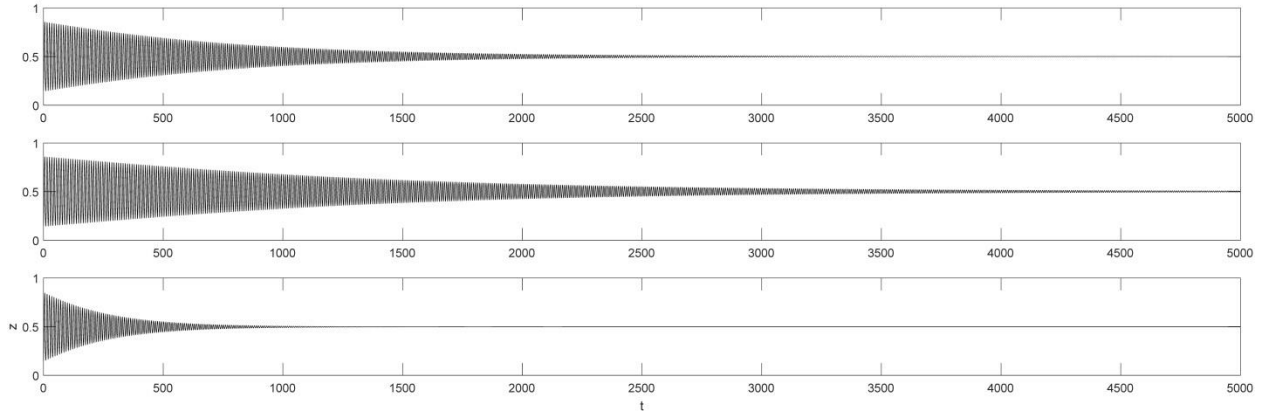
994

995

996

997

998



999

1000 Figure 9. For the “reversed flow” experiment (Experiment 1e in Table 1), z-position of a sample
 1001 particle trajectory as function of time for 3 values of Ω : 0 (top), 0.6 (middle), and 2 (bottom).

1002 Time t is in dimensionless units (but since our scaling coefficient for time is equal to 1 sec, the
 1003 numbers on the x-axis can also be read as dimensional time in sec.)

1004

1005

1006

1007

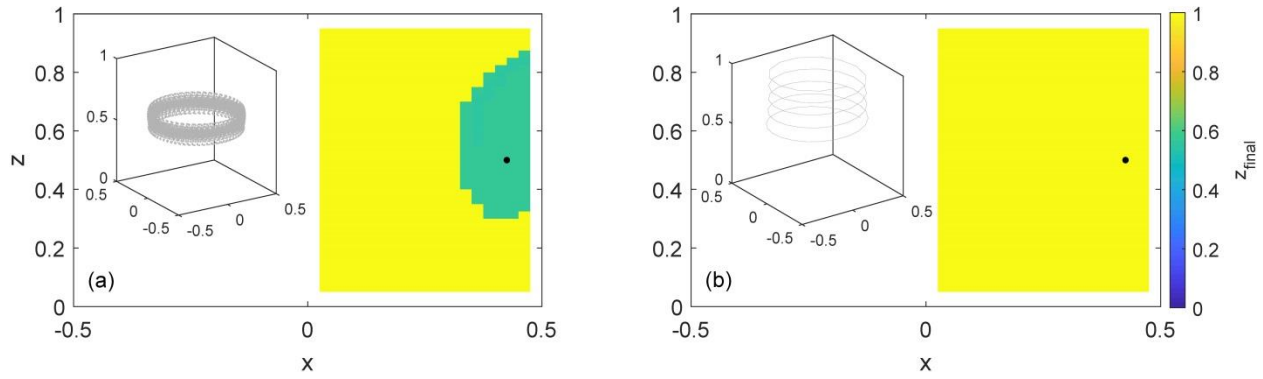
1008

1009

1010

1011

1012



1013

1014 Figure 10. For the “slow overturn” Experiment 1c from Table 1, color indicates the final z-
 1015 coordinate of a particle’s trajectory at the end of integration time as a function of particle’s
 1016 release location for 2 values of d : (a) 5×10^{-4} and (b) 10^{-3} . Yellow corresponds to particles
 1017 rising up to the top, whereas green indicates the basin of attraction of the subsurface attracting
 1018 periodic orbit. The insets at the left side of each frame show a sample trajectory whose release
 1019 location is indicated by the black dot.

1020

1021

1022

1023

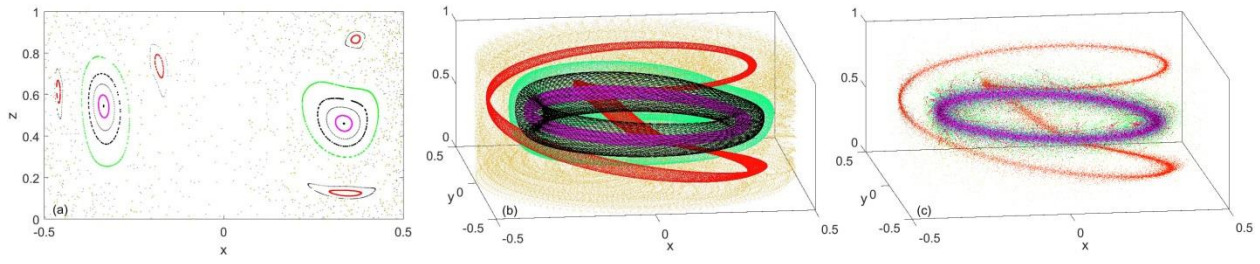
1024

1025

1026

1027

1028



1029

1030 Figure 11. Same as Fig. 2(d-f) but with $b = 3.8$.

1031

1032

1033

1034

1035

1036

1037

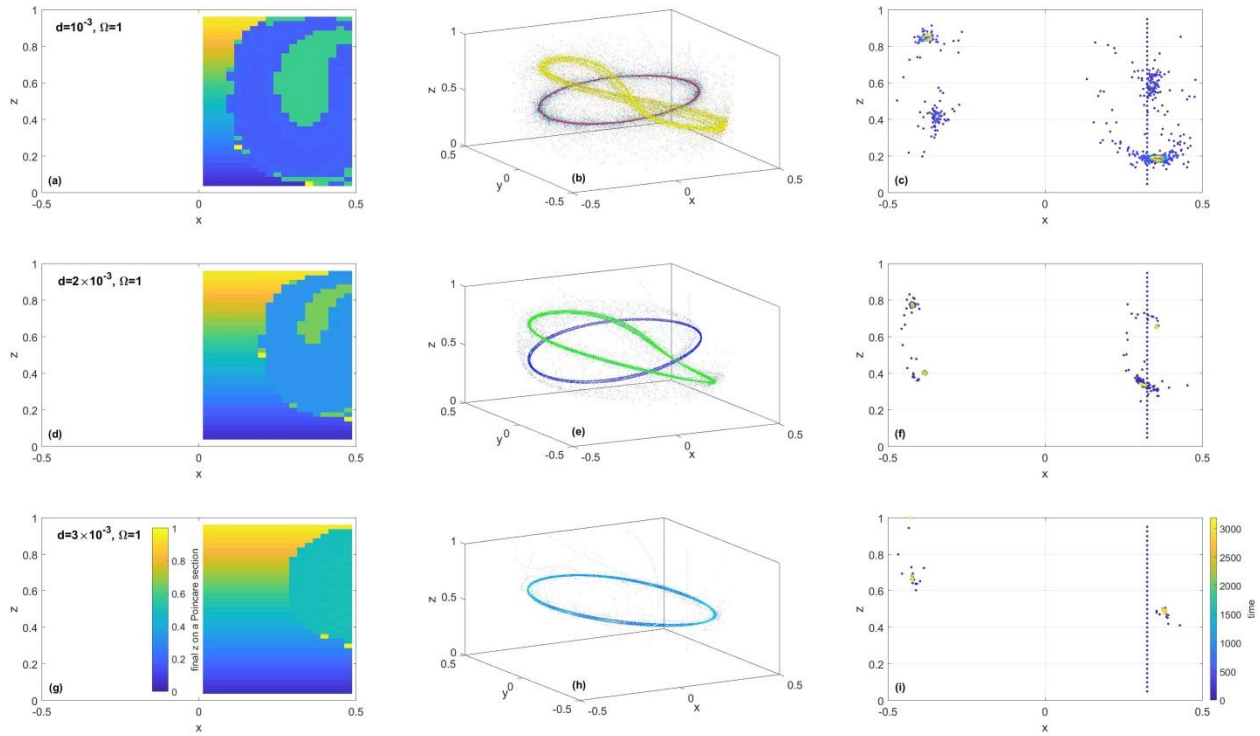
1038

1039

1040

1041

1042



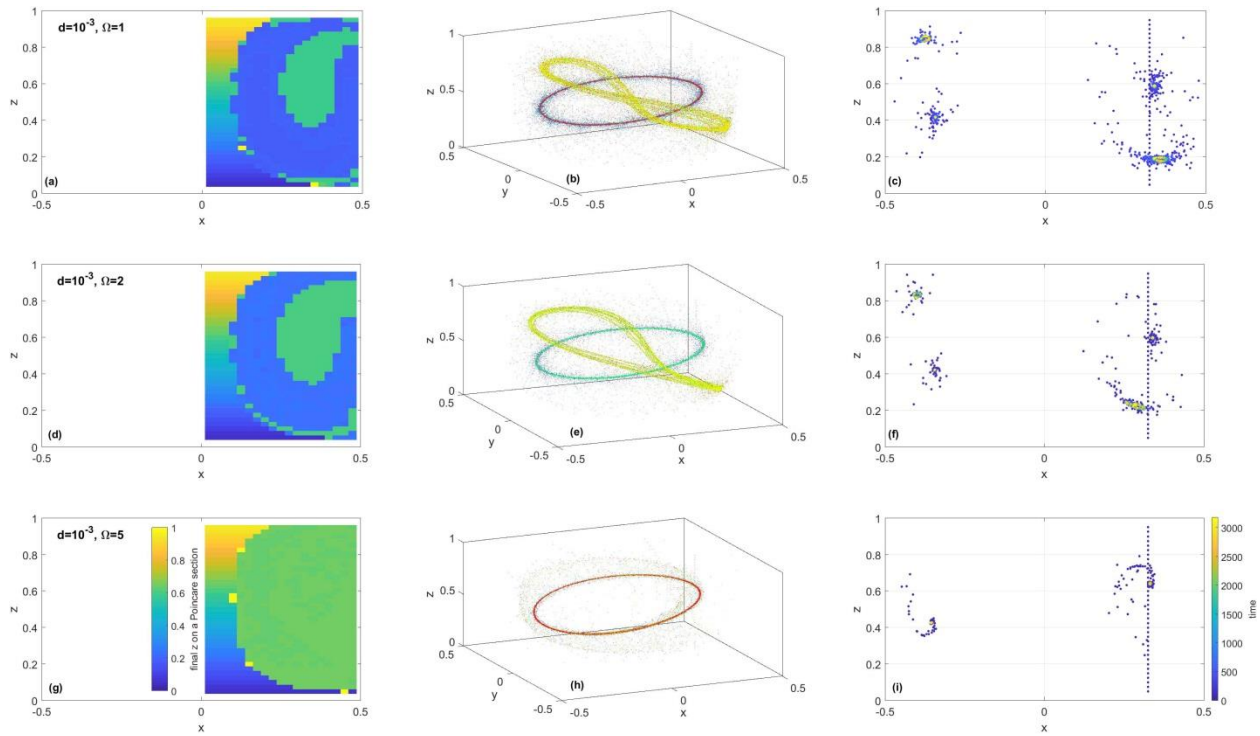
1043

1044 Figure 12. For the steady perturbed system (Experiment 2 in Table 1), changes in the location of
 1045 the attracting periodic orbits, basins of attractions, and time of attraction as a function of particle
 1046 diameter d (and thus $\tilde{\epsilon}$). (a,d,g) show z-coordinate of the last crossing of trajectory with the x-z
 1047 Poincare plane as a function of release location; flat regions are basins of attraction for the 2
 1048 attractors. (b,e,h) show 20 trajectories in 3d released along a vertical line at $y = 0, x = 0.334,$
 1049 $0.05 < z < 0.95$; denser cores indicate attractors. (c,f,i) show crossing of the same select 20
 1050 trajectories with the x-z Poincare plane, color coded by time; blue corresponds to release
 1051 location, yellow corresponds to final positions.

1052

1053

1054



1055

1056 Figure 13. For the steady perturbed system (Experiment 2 in Table 1), changes in the location of
 1057 the attracting periodic orbits, basins of attractions, and time of attraction as a function of frame
 1058 rotation Ω . (a,d,g) show z-coordinate of the last crossing of trajectory with the x-z Poincare plane
 1059 as a function of release location; flat regions are basins of attraction for the 2 attractors. (b,e,h)
 1060 show 20 select trajectories in 3d released along a vertical line at $y = 0, x = 0.334, 0.05 < z <$
 1061 0.95 ; denser cores indicate attractors. (c,f,i) show crossing of the same 20 trajectories with the x-
 1062 z Poincare plane, color coded by time; blue corresponds to release location, yellow corresponds
 1063 to final positions.

1064

1065

1066